Reconfigurable Multiport Solid-State Transformer for DC Fast Charging Stations

by

Ruvini Wathsala De Seram Edirisooriya Mohottige

A thesis submitted to the
School of Graduate and Postdoctoral Studies in partial
fulfillment of the requirements for the degree of

Master of Applied Science in Electrical and Computer Engineering

Faculty of Engineering and Applied Science

Department of Electrical, Computer, and Software Engineering

University of Ontario Institute of Technology (Ontario Tech University)

Oshawa, Ontario, Canada

Mar 2025

THESIS EXAMINATION INFORMATION

Submitted by: **Ruvini Wathsala De Seram Edirisooriya Mohottige**

Master of Engineering and Applied Science in Electrical Engineering

Reconfigurable Multiport Solid-State Transformer for DC Fast Charging Stations

An oral defense of this thesis took place on March 06, 2025, in front of the following examining committee:

Examining Committee:

Chair of Examining Committee	Dr. Akramul Azim
Research Supervisor	Dr. Sheldon Williamson
Examining Committee Member	Dr. Tarlochan Sidhu
Thesis Examiner	Dr. Bale Reddi

The above committee determined that the thesis is acceptable in form and content and that a satisfactory knowledge of the field covered by the thesis was demonstrated by the candidate during an oral examination. A signed copy of the Certificate of Approval is available from the School of Graduate and Postdoctoral Studies.

ABSTRACT

This thesis presents a Solid-State Transformer (SST)-based Electric Vehicle (EV) fast charging station that enhances reliability and optimizes power distribution. Traditional SST-based stations rely on a shared DC bus, susceptible to faults that disrupt the entire system. The proposed system introduces multiple independent DC buses, isolating faults and improving reliability while eliminating the need for additional DC-DC converters, reducing costs and space. Reconfigurable ports deliver 800V, 400V, and 200V, accommodating heavy, medium, and light EVs. A dynamic reconfiguration algorithm adjusts the ports based on vehicle requirements. MATLAB/Simulink simulations confirm stable charging currents and voltages under varying loads. A scaled-down prototype achieves an efficiency of 93.75%, with experimental results showing light EVs charged at 1.25A/50V and heavy EVs at 2.5A/100V, with an 8.2% voltage ripple. Grid current THD remains below 5%, meeting IEEE 519-2022 standards. The system enhances EV fast charging stations' reliability, efficiency, and cost-effectiveness.

Keywords: Solid-state transformer; Reconfigurable charging station; DC fast charging; Multiport EV charging

AUTHOR'S DECLARATION

I hereby declare that this thesis consists of original work of which I have authored. This is a true copy of the thesis, including any required final revisions, as accepted by my examiners.

I authorize the University of Ontario Institute of Technology (Ontario Tech University) to lend this thesis to other institutions or individuals for the purpose of scholarly research. I further authorize the University of Ontario Institute of Technology (Ontario Tech University) to reproduce this thesis by photocopying or by other means, in total or in part, at the request of other institutions or individuals for the purpose of scholarly research. I understand that my thesis will be made electronically available to the public.

Ruvini Edirisooriya Mohottige

STATEMENT OF CONTRIBUTIONS

Journal Papers

R. De Seram, K. T. Lulbadda, Oruganti V.S.R.Varaprasad and S. S. Williamson. "Reconfigurable Multiport Solid-State Transformer for DC Fast Charging Stations", IEEE Journal of Emerging and Selected Topics in Power Electronics (JESTPE), December 2024. (Under Review)

A. Golder, K. Lulbadda, **R. De Seram**, T. Sidhu; S. Williamson, "Rule-Based Energy Management System for Vehicle-to-Vehicle Power Sharing", *IEEE Transactions on Industry Application (IAS)*, August 2024. (Under Review)

Prints

K.T. Lulbadda, A. Golder and **R. De Seram,** "Chapter 5: Electric Vehicle as Decentralized Energy Storage System," in *Technologies and Applications of Batteries, Smart Charging, and Advanced Battery Management Systems for E-mobility*, A. Samanta and S. Williamson, River Publishers, 2024. (Under Review)

K.T. Lulbadda, A. Golder and **R. De Seram,** "Smart Grid Communication and Protocols and Smart Integration of EVs," *in Electric Vehicle and Distributed Generation - Microgrid*, A. Samanta and S. Williamson, River Publishers, 2024. (Under Review)

Conference Proceedings

R. De Seram, A. Golder, and S. S. Williamson, "Recent Advancements in Solid State Transformer-based EV Fast Charging Stations," 2023 IEEE 14th International Conference on Power Electronics and Drive Systems (PEDS), Montreal, QC, Canada, 2023, pp. 1-6.

R. De Seram, K. T. Lulbadda, T. Sidhu and S. S. Williamson, "A Solid-State Transformer-based Charging Station for Catering Heavy/Medium and Light Electric Vehicles," 2024 4th International Conference on Smart Grid and Renewable Energy (SGRE), Doha, Qatar, 2024, pp. 1-6.

R. De Seram, K. T. Lulbadda, T. Sidhu and S. S. Williamson, "A Quad-Active Bridge (QAB)-Based Solid-State Transformer for Fast Charging of Light/Medium and Heavy Electric Vehicles," *2024 IEEE International Conference on Industrial Technology (ICIT)*, Bristol, United Kingdom, 2024, pp. 1-6.

R. De Seram, K. T. Lulbadda, T. Sidhu and S. S. Williamson, "An In-depth Comparative Analysis and Efficiency Evaluation of Dual- and Quad-active Bridge for Solid State Transformer Applications," *2024 IEEE Transportation Electrification Conference and Expo (ITEC)*, Chicago, IL, USA, 2024, pp. 1-6.

K. T. Lulbadda, **R. D. Seram**, T. Sidhu, and S. S. Williamson, "Analysing the Behavior of Solid State Protection System for Dual Active Bridge in Solid State Transformers Under Short Circuit Faults", IEEE Energy Conversion Congress & Expo (ECCE), Phoenix, Arizona, USA, 2024. (Presented)

R. De Seram, K. T. Lulbadda, Oruganti V.S.R.Varaprasad, and S. S. Williamson, “An Analysis of Single- and Dual-Phase Shift Modulation Techniques for Closed-loop Control of Dual-Active Bridge”, *Annual Conference of the IEEE Industrial Electronics Society (IECON)*, Chicago, Illinois, USA, 2024 - to be presented in November 2024.

ACKNOWLEDGEMENTS

The creation of this master's thesis has outlined a trajectory marked by both academic progress and personal evolution for me. At this juncture, I wish to express my profound gratitude to all those who have lent their support and guidance throughout this undertaking. Primary among them is my esteemed supervisor and thesis advisor, Dr. Sheldon Williamson, to whom I extend my sincere gratitude and deepest appreciation for his continuous guidance, sustained support, and immense encouragement that have significantly shaped the entirety of the research process. His valuable feedback and unwavering commitment have played an instrumental role in directing the course of this scholarly endeavor.

I would also like to extend my gratitude to my esteemed colleagues and companions in the STEER group, whose collective encouragement, support, and assistance have served as a constant throughout this scholarly odyssey. Engaging in intellectual discussions and brainstorming sessions along with getting timely feedback from this group has undeniably contributed substantially to the refinement of my ideas. Again, I would like to thank Dr. Sheldon Williamson and all STEER members for always making me feel at home and helping me throughout this academic journey. A profound acknowledgment is also due to my beloved family members, who deserve heartfelt thanks for their unconditional love, moral support, and huge encouragement. They have been a consistent source of motivation and strength, and I am genuinely appreciative of all the sacrifices and hard work they have carried out to facilitate my academic journey.

Lastly, I would also like to acknowledge and extend my thankfulness to UOIT for providing me with the proper facilities and lab space to conduct my research study.

TABLE OF CONTENTS

LIST OF TABLES

CHAPTER 1

CHAPTER 2

LIST OF FIGURES

CHAPTER 1

CHAPTER 2

CHAPTER 3

CHAPTER 4

LIST OF ABBREVIATIONS AND SYMBOLS

AC	Alternating Current
AI	Artificial Intelligence
AWG	American Wire Gauge
CHB	Cascaded H Bridge
CS	Current Source
DAB	Dual Active Bridge
DC	Direct Current
DCFC	Direct Current Fast Charging
DER	Distributed Energy Resources
DPS	Dual Phase Shift
EMI	Electro Magnetic Interferences
EPS	Extended Phase Shift
ESS	Energy Storage Systems
EV	Electric Vehicle
FCS	Fast Charging Station
G2V	Grid-to-Vehicle
FFT	Fast Fourier Transform
HF	High-Frequency
HV	High Voltage
IGBT	Insulator Bipolar Gate Transistor
IMPT	Individual Module Power Transmission
ISOP	Input Series Output Parallel
LFT	Low-Frequency Transformer
LV	Low-Voltage
MMC	Modular Multi-level Converter
MOSFET	Metal Oxide Semi-conductor Field Effect Transistor
MV	Medium Voltage
NPC	Neutral Point Clamp
PCC	Point of Common Coupling
PV	Photo Voltaic
PWM	Pulse Width Modulation
QAB	Quad-Active Bridge
SAE	Society of Automobile Engineers
SoC	State of Charge
SPS	Single Phase Shift
SST	Solid-State Transformer
THD	Total Harmonic Distortion
TPS	Tripple Phase Shift
V2G	Vehicle-to-Grid
V2V	Vehicle-to-Vehicle

XFC	Extra Fast Charging
ZVS	Zero Voltage Switching

Chapter 1 Introduction

The global energy demand for charging Electric Vehicles (EV)s is projected to rise significantly, reaching approximately 800 TWh, as highlighted in [1]. To facilitate the widespread adoption of EVs, DC fast charging stations (FCS) are increasingly being deployed, driven by their ability to significantly reduce charging time, enhance convenience, and extend EV range more efficiently. To support this shift, it is essential to develop charging infrastructures capable of accommodating various EV clusters, including heavy-duty, medium-duty, and light-duty vehicles. According to the SAE J1772-2017 standard, EV charging is categorized into four levels: AC Level 1, AC Level 2, DC Level 1, and DC Level 2. While AC Levels 1 and 2 are intended for slow charging, offering power capacities up to 19.2 kW with operating voltages of 120V and 240V AC respectively, DC charging supports fast charging with power capabilities up to 400 kW and above and voltage levels as high as 1000V [2].

However, this growing demand for EV charging poses substantial challenges to the power distribution network, including increased peak demand and deterioration of power quality [3], [4], [5]. To address these challenges, FCS is integrating renewable energy sources such as photovoltaic (PV) and energy storage systems (ESS). While these measures help mitigate peak demand, they introduce problems related to power stability and quality [6], [7].

Traditional low-frequency transformers (LFT) have inherent limitations in managing these issues related to high power requirements, and significant demand variations effectively [8]. Consequently, the focus has shifted to replacing bulky LFTs with compact solid-state transformers (SST), which offer a promising solution. SST-based fast charging stations have emerged as a compact and efficient solution due to their high-frequency (HF) operation, enabling reduced transformer size [9]. SSTs provide key advantages over conventional transformers, including smart functionality, enhanced grid compatibility, bidirectional power flow, and high-power delivery for faster EV charging, making them a promising technology for future charging stations.

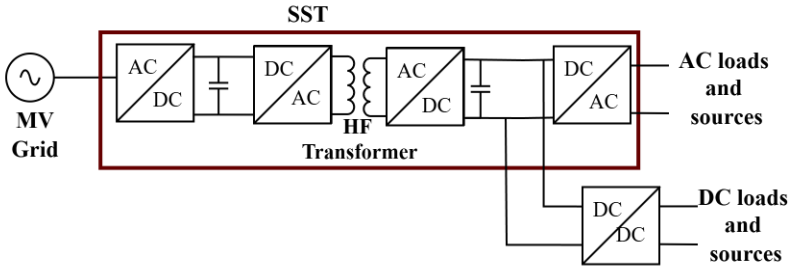

Figure 1: General architecture of SST application

The conventional arrangement of an SST-based power system illustrated in Figure 1, integrates a high-frequency transformer with multiple power electronic converters to form a compact system directly interfaced with the Medium Voltage (MV) grid. This configuration, incorporating DC links between power conversion stages, enables advanced functionalities such as power factor correction, voltage sag compensation, and power quality improvement [10]. Additionally, it facilitates the seamless integration of DC loads like EVs and DC sources such as PV systems and ESS without requiring additional conversion stages. The inclusion of a back-end inverter for reconnection to the AC distribution grid further enhances the system's versatility. Its bidirectional power transfer capability facilitates applications such as vehicle-to-grid (V2G) operations. Beyond improving power density, this SST architecture delivers a suite of functionalities that position it as an optimal solution for modern power distribution networks [11].

1.1 EV Fast Charging Stations with Line-Frequency Transformers - Challenges

The EV FCS designed for commercial EV fleets requires total power capacities in the range of several MVAs. These high-power demands necessitate connection to the MV grid through power transformers with correspondingly high-power ratings, further emphasizing the importance of robust and efficient grid infrastructure for widespread EV adoption [15].

FCS can be configured using either an AC bus or a DC bus as depicted in Figure 2 [16]. In the AC bus configuration, the station connects to the MV grid through an MV-Low Voltage (LV) transformer, with each charger comprising a rectifier and a DC-DC converter to charge EVs. In the DC bus configuration, chargers connect to the grid via an MV/LV

transformer and a common DC bus created by a rectifier, from which DC-DC converters supply power to the EVs for charging their batteries. The DC bus system is more efficient due to a reduced number of power electronics converters and enhanced isolation between rectification and DC-DC conversion stages, offering greater flexibility in power ratings, improved handling of grid instability, and reduced control complexity [17], [18].

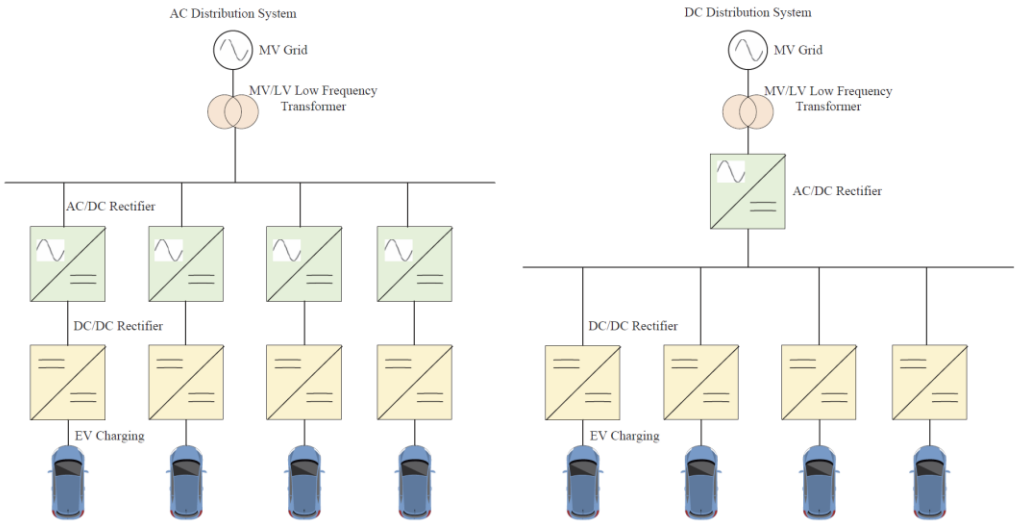

Figure 2: Different configurations of LFT-based FCS

In both the AC and DC bus configurations, fast-charging stations connect to the grid through MV/LV transformers. However, the integration of such transformers introduces specific challenges. Studies outlined in [19], [20], [21] review various technologies available for FCS and highlight key limitations of traditional LFTs. LFTs are inefficient at managing multiple voltage levels and require additional converters and equipment for integration with renewable energy sources and ESS, thereby increasing system complexity. Due to the intermittent nature and large-scale charging demands in FCSs, it may result in increased daily demand peaks, transformer overloading and its accelerated aging, feeder overloading, increased power losses, and power quality issues including voltage sags and swells in the host power networks [22].

Research in [23], [24] utilized Monte Carlo simulations to assess the impact of fast-charging stations on the grid, while [25] focused on evaluating the performance of power converters in such applications. These studies reveal that power electronics converters contribute to power quality challenges, including harmonics and voltage instability, which

negatively affect the distribution grid [26]. Moreover, LFTs are inadequate for handling these power quality issues, especially in high-demand scenarios associated with fast charging. They also lack the capabilities for advanced functionalities like voltage regulation, reactive power compensation, and bidirectional power flow, which are critical for seamless integration with smart grids and modern energy systems[27]. Additionally, their large size and weight pose significant physical constraints in high-power applications like EV fast-charging stations.

Replacing LFTs with SSTs is a promising solution to these challenges. SSTs leverage power electronic devices and HF transformers to efficiently operate at the required voltage and frequency, effectively addressing the limitations of traditional LFTs and enhancing the overall performance of fast-charging stations.

1.2 EV Fast Charging Stations with Solid-State Transformers

As described above, the usage of LFT in an EV fast charging station has its limitations related to size, weight, intelligence, and controllability. Since the HF transformer in the SST realizes the benefit of volume and size reduction in the complete charging system, replacing the LFT in the charging station with an SST, aids in resolving these concerns. Additionally, the SST offers several beneficial functionalities over a conventional LFT which include:

1) Voltage disturbance rejection in both the load side and power supply system side
2) Additional voltage regulation
3) Bi-directional power flow control
3) Ability to integrate Distributed Energy Resources (DER) and ESS to the DC port
4) Fault isolation
5) Superior controllability/status monitoring interface
6) Power quality improvement [28], [29].

1.2.1 Challenges of SST-based Systems Compared to Traditional Transformers

SST-based systems present several challenges compared to traditional transformer-based systems, particularly in cost and reliability. One major drawback is the high initial investment required for SST technology, as it relies on advanced semiconductor

components, power electronics, and complex control mechanisms, making it significantly more expensive than conventional transformers. Additionally, SSTs are more sensitive to electrical and thermal stress, increasing the risk of failures and reducing overall reliability. In contrast, traditional transformers have a well-established track record of robustness and long service life. The intricate design and dependence on sophisticated software also introduce potential vulnerabilities, such as cyber threats and control system failures, further complicating their adoption.

Despite these challenges related to cost and reliability, SSTs offer significant advantages that often outweigh their drawbacks. Their ability to enhance power quality, enable bi-directional power flow, and improve fault-tolerant capabilities makes them a promising alternative to traditional transformers, especially in modern smart grids and renewable energy applications.

1.2.2 Topologies of SST

SST is a power electronic device that performs the functionalities of a traditional transformer through power electronics components integrated with an HF transformer and advanced control systems. Considering the configurations described in the literature, SST can be classified into three categories 1) single-stage 2) two-stage, and 3) three-stage as shown in Figure 3 [30].

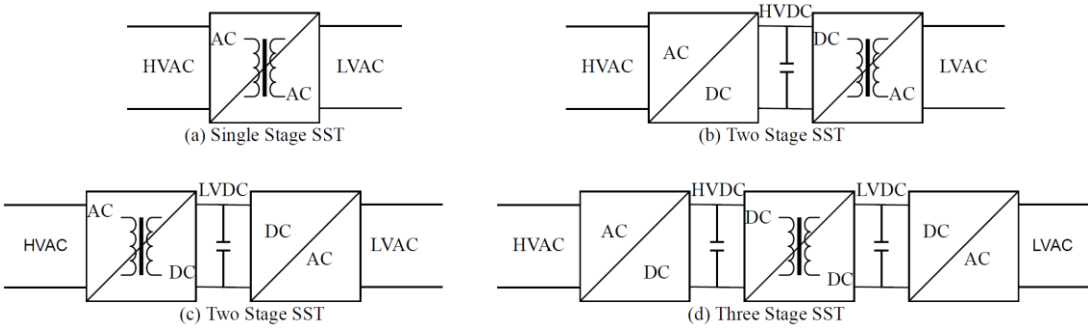

Figure 3: Classification of SST topologies

In the single-stage SST, an AC-AC converter is used in the front end to convert the low-frequency AC to high-frequency AC which is subsequently fed to the HF transformer to convert to low voltage. Then the output of the HF transformer is converted to low-frequency AC. The biggest drawback of this design is the absence of the DC link. In the

two-stage SST, a DC link is present at either the LV side or the HV side of the SST. Three-stage SSTs are the most popular configuration; they have DC linkages on both the LV and HV sides, allowing LV or HV DC equipment to be connected directly to the SST and ensuring power factor correction capability as well. This configuration consists of a rectifier, an isolated DC-DC converter, and an inverter and it is superior to the other two configurations in terms of limiting high currents, power factor improvement, and voltage regulation [31].

1.3 Problem Statement

With the rapid expansion of EV adoption, the demand for efficient, reliable, and scalable EV fast-charging infrastructure is growing exponentially. Traditional SST-based EV FCS face significant challenges in managing the dynamic power requirements of different EV types (light, medium, and heavy EVs). Most existing SST-based EV fast charging stations rely on a common DC bus shared among EVs, with several DC-DC converters managing the power distribution [12].

However, this approach introduces a significant drawback: a single point of failure. A fault in the common DC bus can affect all connected chargers, leading to widespread outages and complicating fault isolation and repair [13]. A fault in the DC bus or its associated components (i.e. a busbar or connectors) can compromise the entire station's functionality, limiting the redundancy of the charging station. Other issues of sharing a common DC bus among all the chargers include maintenance complexity, compatibility challenges, and lack of modular operation.

Furthermore, shared DC bus systems require sophisticated protection mechanisms and additional DC-DC converters to provide varying voltage levels at each port, increasing complexity, cost, and space requirements [14]. As the number of connected chargers increases, the common DC bus must handle higher power levels, which can strain the system's design limits and reduce overall scalability.

Additionally, current DC fast charging stations often have ports configured to deliver a specific charging voltage and current, tailored to EV requirements. When no vehicle matching those specifications is available, the port remains idle, rendering the charger

temporarily unusable. This rigidity leads to underutilized resources, reduced efficiency, and an inability to serve the diverse charging needs of various EV types. These limitations highlight the need for more adaptable and intelligent systems to optimize resource utilization and accommodate varying demands.

Addressing these limitations is essential to develop a flexible, reliable, and future-ready EV charging infrastructure capable of meeting the growing demand and diverse needs of modern electric vehicles.

1.4 Motivation

The proposed research is driven by the need to address the critical challenges outlined in the problem statement and advance EV charging infrastructure. Leveraging the modular structure of SST, the independent operation of charging ports can be achieved, significantly enhancing the reliability and flexibility of DC fast charging stations. By utilizing the isolated nature of Dual-Active-Bridge (DAB) modules within the SST, this research is motivated to create isolated charging ports, thereby mitigating the risks associated with common DC bus architectures and eliminating single points of failure to ensure greater fault tolerance. Additionally, removing dedicated DC-DC converters per port offers a cost-effective and space-efficient solution. Additionally, dynamic reconfiguration of charging ports is a key motivator, as it maximizes resource utilization by preventing idle ports caused by fixed configurations. These motivations underscore the potential of this research to deliver a robust, scalable, and future-ready charging infrastructure.

1.5 Thesis Outline

This thesis is outlined as follows.

Chapter 1: Introduction

Chapter 2: Background and literature review

Chapter 3: Design of the Proposed Reconfigurable Multiport SST for DC Fast Charging Station

Chapter 4: Simulation and Experimental Validation

Chapter 5: Conclusion and Future Works

Chapter 2 Background and Literature Review

Understanding the various SST topologies and their integration into SST-based FCS is critical to advancing this technology. This chapter explores the latest developments in SST technologies for FCS applications, providing insights into their potential to revolutionize EV charging infrastructure.

2.1 Conventional Configuration and the Converters

Figure 4 illustrates the typical structure of an SST-based EV FCS, comprising a front-end AC-DC active rectifier and an isolated DC-DC converter. The isolated DC-DC converter establishes an LV DC link, which facilitates connections to multiple EVs via additional DC-DC converters [32]. An AC port is realized by integrating an inverter with the LV DC link. In the SST architecture, the front-end AC-DC active rectifier and the back-end isolated DC-DC converter serve as critical components. Advanced power electronic converter designs are extensively proposed and validated within the domain of SST technology in the recent literature. To accommodate the voltage and current requirements of power semiconductor devices, these converters frequently adopt a modular design approach.

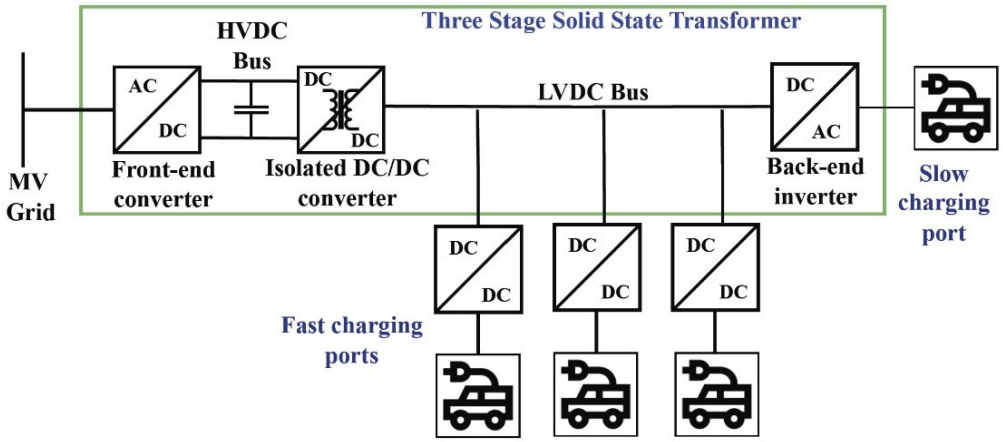

Figure 4: Typical structure of SST-based EV fast charging station

2.1.1 Front-end AC-DC Converter

The front-end converter in an SST-based EV FCS plays a pivotal role as it interfaces directly with the MV grid. This stage is often implemented using modular converter designs, enabling high-power transfer while maintaining reasonable current stress on the

grid side. Various studies, such as [33], [34], [35] have proposed the Modular Multilevel Converter (MMC) for connecting the SST to the MV grid, offering the advantage of an additional MVDC bus. However, the MMC's practical application faces challenges, including high control complexity and the cost of large capacitors required for the MVDC bus. Another solution, a Neutral Point Clamped (NPC) converter was introduced in [36] which reduces the number of power electronic components. Despite this advantage, it encounters difficulties in maintaining power quality under low current or low load conditions. Among the modular AC-DC configurations, the Cascaded H-Bridge (CHB) converter has emerged as the most commonly adopted solution [37], [38], [39]. The CHB converter is favored for its simple control and modulation, as well as its ability to minimize total harmonic distortion (THD). However, this configuration requires a substantial coupling inductor, which can add to the overall system cost and complexity.

2.1.2 Isolated DC-DC Converter

The DC-DC converter within an SST system integrates an HF transformer coupled with power electronic converters on both its primary and secondary sides. The HF transformer ensures galvanic isolation between the SST's input and output. Among the various configurations, the DAB converter is widely utilized in SST applications due to its advantages, including bidirectional power transfer, soft switching, high power density, and straightforward control architecture [40], [41]. To further enhance the power density, the Quad-Active-Bridge (QAB) converter has been proposed in studies [42], [43], [44] This design employs a multi-winding HF transformer that connects three primary sides to a single secondary side, effectively replacing three DAB units in an SST. However, the QAB presents challenges, such as tripling the power ratings required for the secondary switches and transformer windings, which limits its practicality. Additionally, research [45], [46] has introduced matrix converter-based AC-DC DAB modules for SST applications. While these configurations eliminate the need for an MVDC link, they also result in the inability to perform power factor correction, restricting their effectiveness in real-world implementations.

2.2 Existing SST-based EV Fast Charging Station Configurations

In this section, several converter architectures for SST-based EV FCS proposed by researchers are explained and the main features are discussed with pros and cons.

2.2.1 DAB converter-based Topology

Figure 5 provides a detailed schematic of a typical SST-based EV FCS [32], [47]. The system employs a CHB converter for AC-DC conversion and a DAB converter for DC-DC

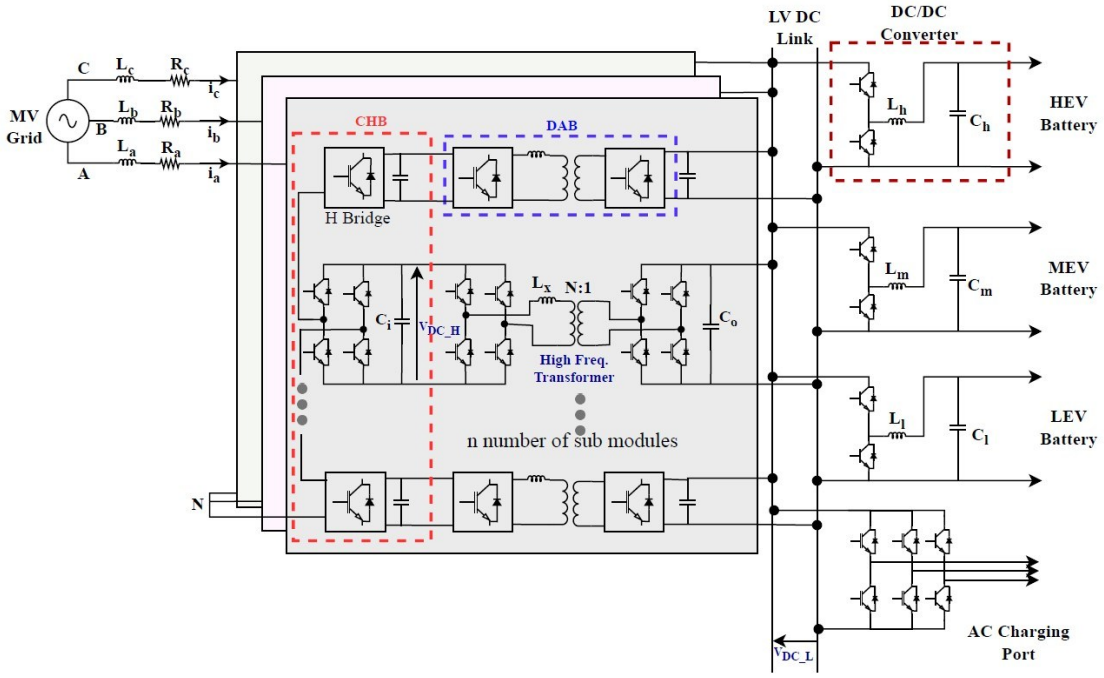

Figure 5: Typical structure of SST-based EV fast charging station

conversion. Multiple H-bridge modules in the CHB generate regulated DC voltages, which serve as inputs to the DAB converters. Input inductors (L_a, L_b, L_c) act as filters, while capacitors (C_i) smoothen the DC outputs. Each CHB output connects to a DAB, comprising two H-bridge converters linked by the HF transformer with added leakage inductance (L_x) for improved performance. The DAB outputs are paralleled to form the LVDC link, further stabilized by an output capacitor (C_o). For fast charging, the LVDC link powers buck-boost converters that provide three voltage levels for heavy, medium, and light EV charging ports. Additionally, a Level II AC charging port is created by connecting the LVDC link to the load via a DC-AC converter. Even though this is the basic architecture for SST integrated

EV charging station, the configuration suffers from a large component count which causes reduced efficiency.

2.2.2 QAB converter-based topology

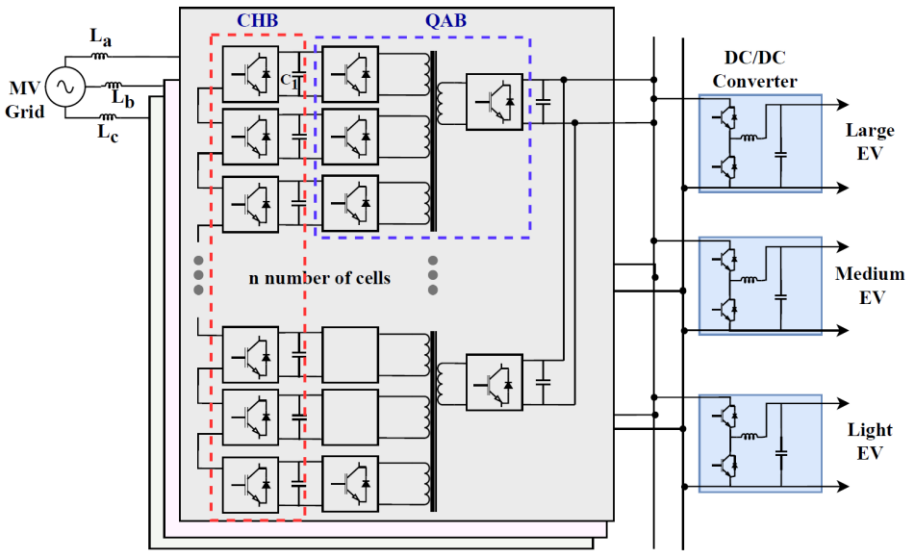

Figure 6: QAB converter-based configuration for SST-based EV fast charging station

A refined SST topology is proposed in [43], [48], utilizing QAB for DC-DC conversion with isolation, as shown in Figure 6. The QAB converter integrates four active H-bridges through a single four-winding transformer, reducing the number of transformers by one-third compared to DAB configurations. This design achieves a 10% reduction in transformer core material due to magnetic coupling among the cells, leading to lower system costs and improved efficiency. While QAB improves power density, it increases the current ratings of the secondary converters, leading to higher costs than DAB-based designs. Additionally, the QAB system lacks the reliability offered by DAB-based configurations. In Input-Series-Output-Parallel (ISOP) architectures, multiple parallel-connected DAB converters power the LV DC link, providing enhanced fault tolerance and system reliability compared to the single-transformer design of QAB.

2.2.3 Matrix Converter-based Topology

The authors in [46] propose a matrix converter for the SST-based FCS, enabling direct line-frequency AC to HF AC conversion at the front end, interfacing the grid through an MVAC-LVDC conversion stage as shown in Figure 7. This design eliminates the bulky HV-side

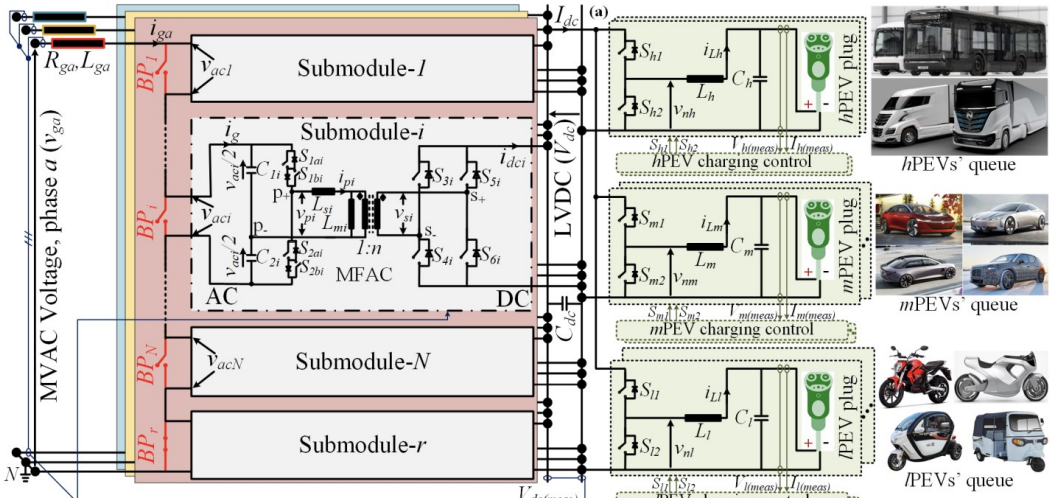

Figure 7: Matrix converter-based topology

DC link capacitor by outputting an HF sinusoidal AC signal, making the system more compact. However, it introduces complex control requirements due to the matrix converter arrangement and imposes higher voltage stress on switches. Additionally, the absence of a DC link restricts decoupled modulation, limiting power factor correction capabilities.

2.2.4 Semi-modular Topology

The architecture presented in [49] as depicted in Figure 8, adopts a semi-modular design where a single full-bridge rectifier with high-voltage devices is used per phase instead of multiple power electronic converters. This approach significantly reduces the component count, simplifying the system. However, a major limitation of this configuration lies in the practical voltage and current rating constraints of power electronic switches, such as SiC

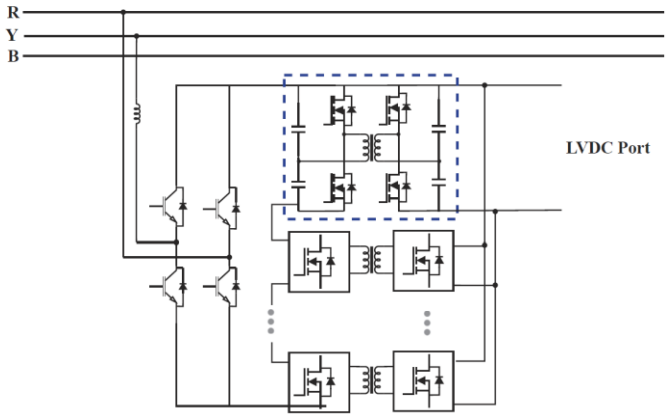

Figure 8: Semi-modular topology

MOSFETs, IGBTs, and GaN devices. Consequently, the front-end converter is unsuitable for high-power applications like EV fast charging stations.

2.2.5 Common Leg Multiport Controller-based Topology

Another configuration proposed in [50] features a current source solid-state transformer (CS-SST) architecture, as illustrated in Figure 9. This design employs a three-leg converter to create two DC ports, thereby minimizing the number of power devices required. The DC ports can be utilized for applications such as EV chargers, ESS, or DER. While this topology benefits from soft-switching capabilities and supports partial power processing, a significant limitation is the shared common leg between the two ports. This design choice compromises isolation and increases vulnerability to faults.

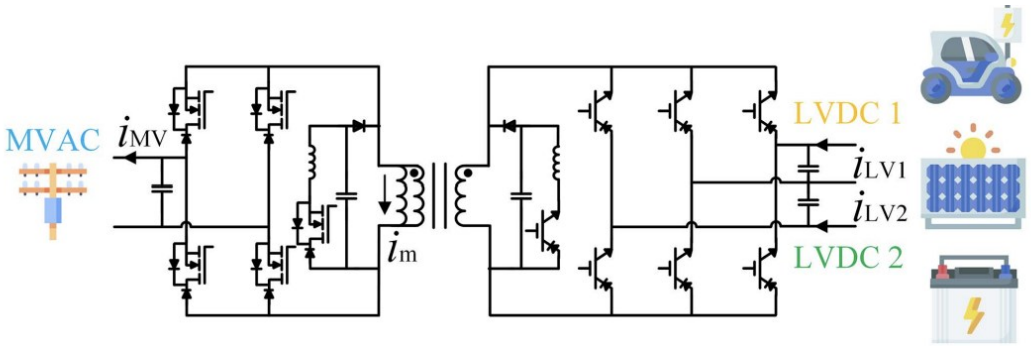

Figure 9: Multiport three-phase converter-based Topology

2.2.6 Individual Module-based Topology

Figure 10 illustrates an EV FCS equipped with multiple DC ports, which are generated either through shared sub-modules of an SST or by utilizing individual sub-modules to support different voltage levels. The authors of [51] propose an Individual Module Power

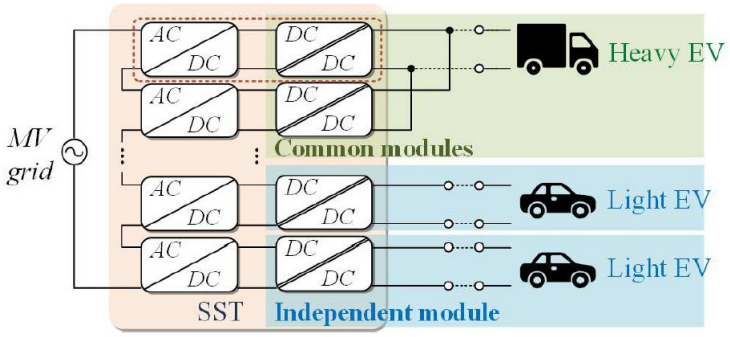

Figure 10: Individual module power transfer topology

Transmission (IMPT) control strategy tailored for Extreme Fast Charging (XFC) stations configured with SSTs. Typically, in SST systems, the power output of individual modules is not independently regulated; instead, the module outputs are connected in parallel to form a DC bus. Consequently, additional DC-DC conversion stages are required to enable simultaneous charging of multiple EVs with different capacities. By employing the IMPT approach, the module outputs of the SST can be directly connected to EVs, eliminating the need for extra power conversion stages. This significantly reduces both construction costs and power losses. In addition, the DC ports are isolated from one another, providing the added advantage of enhanced reliability. However, a critical challenge of this configuration lies in ensuring effective power balance control at the front-end sub-modules of the CHB converter. As a result, the control system for the CHB becomes more complex to design and implement.

Table 1 summarizes the different topologies and comparison of each topology with the proposed topology of this research.

Table 1: Comparison of existing SST-based EV Fast Charging Configurations

Configuration	**Power conversion stages**	**Number of switches per level**	**Efficiency**	**Isolation between ports**	**Reconfig urability**
DAB-based [32], [47]	AC-DC: CHB DC-DC: DAB DC-DC: Buck Boost	14	95%	No	No
QAB-based [43], [48]	AC-DC: CHB DC-DC: QAB DC-DC: Buck Boost	11	N/A	No	No
Matrix-based [46]	AC-AC: Matrix AC-DC: H-Bridge DC-DC: Buck Boost	10	96.4%	No	No
Semi-modular [49]	AC-DC: H-Bridge DC-DC: QAB DC-DC: Buck Boost	7	97.7%	No	No
Common leg Multiport [50]	AC-AC: Matrix AC-DC: Three-leg converter DC-DC: Buck Boost	9	97.4%	No	No
Individual Module-based [51]	AC-DC: CHB DC-DC: DAB	12	N/A	Yes	No
Proposed topology	AC-DC: CHB DC-DC: DAB	12	94.2%	Yes	Yes

2.3 Challenges and Opportunities of SST-based EV Fast Charging Stations

Most of the existing configurations for SST-based EV fast charging stations use a regulated common DC bus shared by the EVs with several DC-DC converters as illustrated in Figure 4. However, one major disadvantage of utilizing a shared DC bus is the occurrence of a single point of failure. A problem in one system component might spread throughout the shared DC bus, impacting all linked chargers. This raises the likelihood of extensive outages and complicates fault isolation and repair procedures. Additionally, sophisticated protection mechanisms are needed to promptly identify and isolate shared DC bus system errors.

Moreover, different DC-DC converters are required at each port to provide different voltage levels for various categories of EVs. For example, the charging station must be capable of accommodating multiple EV battery sizes with varying voltage ratings (for example, trucks and buses with 800V, automobiles with 400V, and three-wheelers and two-wheelers with 200V). The research focus should be to reduce the complexity and cost and optimize the number of devices used in SST-based systems.

The HF transformer in SST plays a major role in reducing the overall size of the system but the thermal management for such compacted system is challenging. Another consideration is the limitation of built-in overvoltage and overcurrent protection for SST. In a charging station, the reliability of the protection scheme is important, and more research should be carried out regarding using solid-state protection devices for an SST-based fast charging station.

2.4 Research Gaps

As discussed above, to address the single point of failure issue, the authors of [51] propose an EV fast charging station with multiple DC buses that are isolated from each other. This configuration ensures that if one bus fails, the others can continue functioning, thereby minimizing the impact on the overall system and increasing reliability. The proposed configuration also contributes to cost and space savings since the additional DC-DC converters needed for each charging port are eliminated.

The major challenge of this configuration is handling the power imbalances in each sub-module of the front-end CHB converter, and the authors have proposed an individual module power transmission controller and have validated by simulation results which is complex to implement in actual hardware.

The system proposed by the authors in [51] maintains a fixed output voltage at each port, limiting its flexibility. As a result, when a port is idle, it cannot be used to supply partial power to another vehicle that has a different power requirement, leading to inefficient resource utilization.

Furthermore, the feasibility of individual module power transfer has only been validated through simulations. However, there is a lack of experimental validation for controlling the power of isolated charging ports without relying on DC/DC converters. These gaps represent key research challenges identified through a comprehensive literature review.

2.5 Research Goals and Objectives

The aim is to create a system capable of efficiently managing the varying power demands of different EVs while ensuring voltage stability, operational reliability, and cost efficiency. The objectives of this thesis are as follows:

- Analysis of existing SST-based EV fast charging systems:
  To conduct an in-depth study of the challenges associated with conventional SST-based EV fast charging stations, focusing on shared DC bus configurations, additional DC-DC converters, and reliability issues, and identify key gaps and limitations.
- Development of independent DC bus architecture:
  To design an innovative EV fast-charging system with independent DC buses for each charging port, addressing the single-point-of-failure issue and enhancing fault isolation and reliability.
- Integration of advanced control features:
  To implement SST-based switching mechanisms that facilitate precise voltage regulation and ensure seamless, independent operation of DC buses for each charging port.

- Design of a dynamic reconfiguration algorithm
  To develop and integrate a dynamic reconfiguration algorithm capable of real-time adjustments to charging power and voltage levels for different EV types, ensuring adaptive charging under varying load conditions.
- System validation and performance evaluation:
  To validate the proposed system through detailed simulations and experimental prototypes.

By achieving these objectives, this thesis aims to provide a reliable, flexible, and cost-efficient solution to the current challenges in EV fast charging infrastructure, supporting the widespread adoption of electric vehicles.

Chapter 3 Design of the Proposed Reconfigurable Multiple DC Buses-enabled Solid-State Transformer for EV Fast Charging Station

The proposed EV FCS proposed by this research is an advanced version of the architecture proposed in [51]. It achieves the following additional enhancements apart from the increased power density and reduced cost.

1. An optimum range of charging voltages is achieved by reconfiguring the system dynamically using additional switches, as per the requirement. A reconfiguration algorithm is proposed to operate these switches dynamically.
2. The decoupled modulation control system is proposed for an easy-to-implement capacitor voltage balancing controller at the CHB converter.
3. A scaled-down prototype of the system and controller is developed and validated by experimental results.

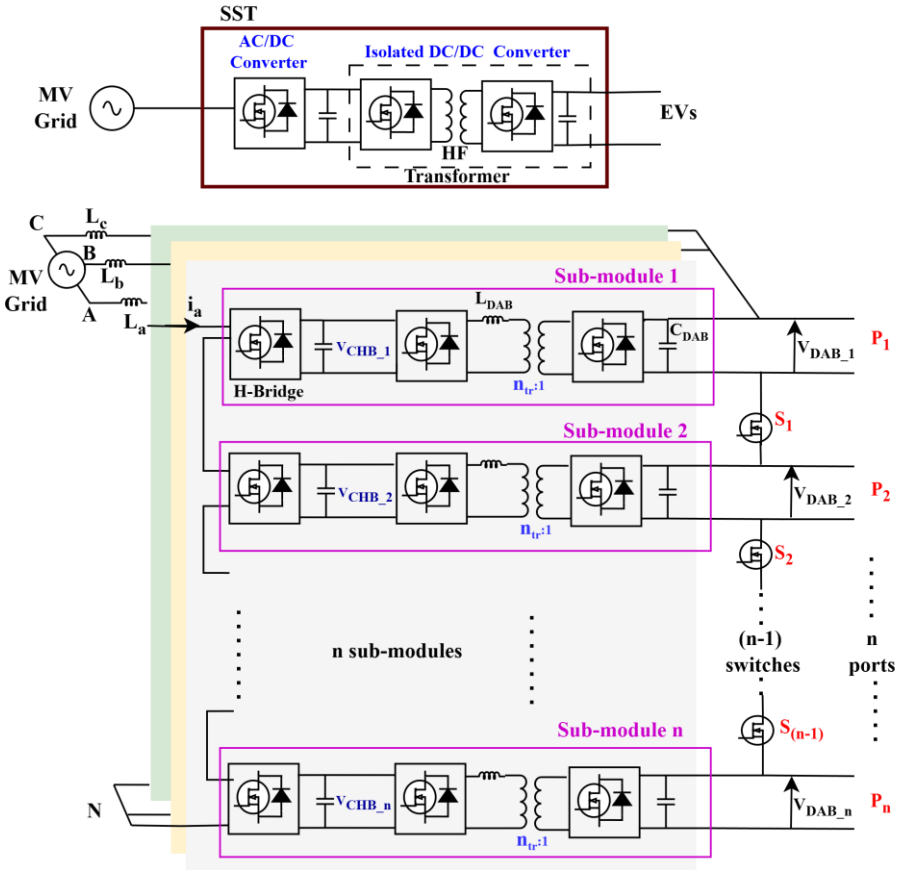

Figure 11: Proposed configuration

A detailed illustration of the proposed EV fast charging station is depicted in Figure 11. The charging station is directly connected to the MV grid. On the front end, a CHB is connected to the MV grid to convert HV AC into DC. L_a, L_b, and L_c are inductors at each phase used as input filters. CHB consists of several H-bridges (sub-modules) connected in series to reduce the voltage stress of power electronic switches. The figure shows n sub-modules at each phase. The output of each sub-module is maintained at a regular DC voltage level (V_{CHB_1} to V_{CHB_n}) and is fed to a DAB converter. The primary bridge of the DAB converts the DC voltage to HF AC voltage and the transformer provides the galvanic isolation and the voltage transformation. The secondary bridge converts the HF AC voltage back to a DC voltage.

As illustrated in Figure 11, each DAB output forms an EV charging port, offering *n* charging points designated as P_1 to P_n. Switches labeled S_1 through $S_{(n-1)}$ are incorporated between each charging port, enabling reconfiguration of the EV charging system. For instance, when switch S_1 is activated, the P_1 and P_2 ports are connected in series to deliver a higher voltage charging port (P_{12}), as demonstrated in Figure 12. This reconfiguration

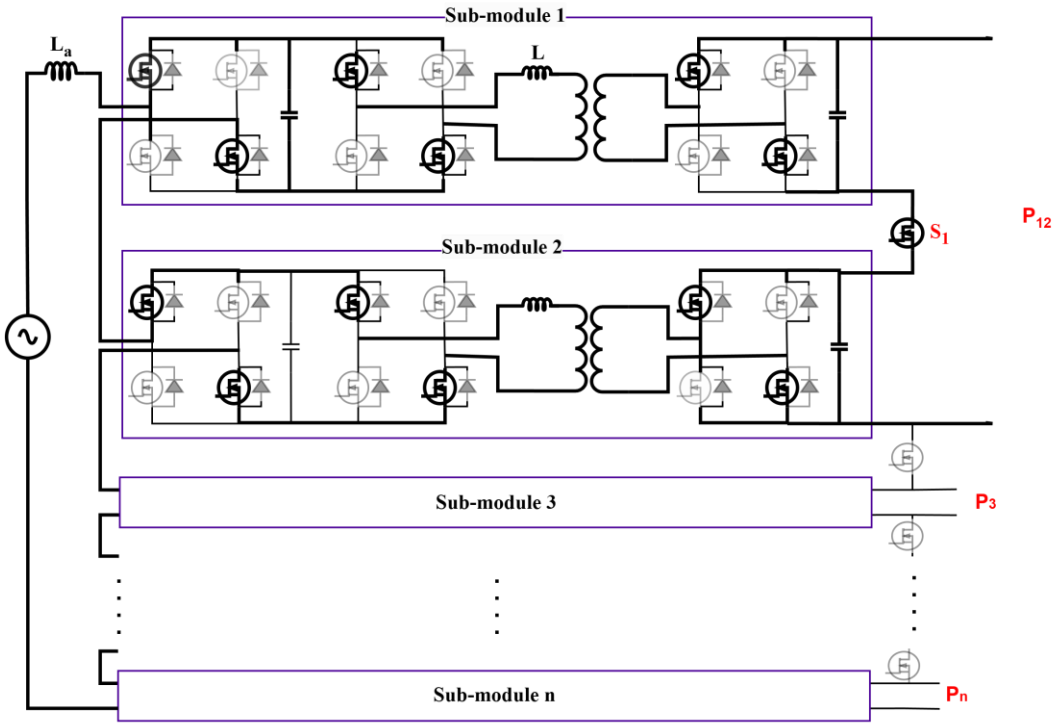

Figure 12: Operation mode when S1 is turned ON

strategy facilitates adaptability, allowing the system to supply low power for smaller EV batteries or reconfigure to deliver higher power for larger EV batteries.

3.1 System Modelling and Designing

The minimal specifications that need to be specified for the SST are:

- Rated power – P_{rated}
- Line-to-line medium voltage – V_{MV}
- EV charging voltage & current – V_{chg} & I_{chg}

Also, the rated voltage and current of the available semi-conductor switches are important parameters in determining the output voltage and the number of sub-modules required at the CHB.

Assumptions made in modeling the system are,

- Ideal components and ideal switching are considered.
- The passive components operate within a linear region and phenomena such as saturation are avoided
- Negligible parasitic effects in components
- Model is developed considering the steady-state operation
- Constant load and source voltage
- Sensors are ideal and there are no delays or inaccuracies

3.1.1 Input Filter Design

The SST is connected to the MV grid through a filter, which serves two critical functions. First, it enables the regulation of active and reactive power exchange between the SST and the grid. Second, it mitigates harmonic distortion caused by the SST. A simple L-filter is often employed to couple the CHB to the MV grid. This filter configuration is preferred for two primary reasons:

1. The CHB's architecture and its modulation strategy result in an increased effective switching frequency as the number of H-bridges grows. This higher frequency, combined with a more sinusoidal waveform generated by additional H-bridges, significantly reduces harmonic distortion and allows for the use of smaller filters

[52], [53]. The highly effective switching frequency supports efficient filtering, while the smaller filter size minimizes voltage drops across the inductor.

2. HV capacitors are cost-intensive components. To optimize system costs, the use of filters with capacitors is avoided wherever feasible.

3.1.2 Design of the CHB Converter

The CHB consists of an input filter, several H-bridges in cascade, and an output filter capacitance for each H-bridge. In the proposed configuration, there are three CHB converters in three phases and Figure 13 illustrates a CHB connected to a single phase. Furthermore, each H-bridge is connected to a control circuit, which switches the power electronic switches ON or OFF to get the desired waveform. The parameters that are required to create a model of the CHB are the number of H-bridges (n), DC-link voltage (V_{CHB}), filter capacitor (C_{CHB}), input filter inductance (L_{CHB}), and switching frequency (f_{S_CHB}).

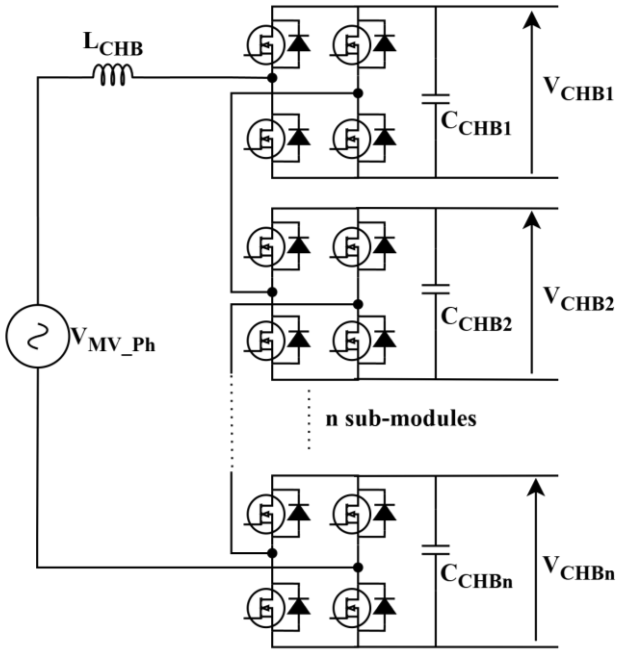

Figure 13: CHB converter configuration

While adding more H-bridges in the CHB enhances the output waveform quality, each additional H-bridge requires a corresponding DAB converter with an HF transformer. This

leads to greater system complexity, increased volume, and higher costs. As a result, it is crucial to minimize the number of H-bridges to achieve an efficient and cost-effective design. If the voltage and current ratings of the selected switch are V_{switch} and I_{switch} respectively, the maximum capacity of the H-bridge ($P_{sub\text{-}module}$) is as follows.

$$P_{sub-module,max} = 2V_{switch} * I_{switch} \quad (3.1)$$

The number of sub-modules can be selected as follows.

$$n_{min} = \frac{\sqrt{2} * V_{MV\_ph}}{V_{CHB-max}} \quad (3.2)$$

Here, V_{CHB_max} is the maximum DC voltage considered at the output of each sub-module which depends on the power rating of power electronic switches. Typically, 80% of the MOSFET rating is considered.

The output capacitor is needed to smooth the DC link voltage. The rectified power per each sub-module can be expressed as,

$$P_{sub-module} = \frac{1}{3} * \frac{P_{rated}}{n} \quad (3.3)$$

Setting a voltage ripple to 10%, the required minimum capacitance can be calculated as follows.

$$C_{CHB,min} = \frac{\frac{1}{3} * \frac{P_{rated}}{n}}{2 * pi * f_{s\_CHB} * (0.1 * V_{CHB}) * V_{CHB}} \quad (3.4)$$

3.1.3 Design of the DAB Converter

The DAB converter is used to achieve galvanic isolation and voltage transformation between the HV and LV sides of the SST. It consists of a DC-AC and AC-DC converter with a high-frequency transformer in between as in Figure 14.

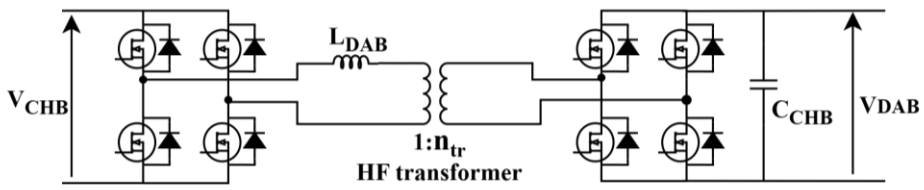

Figure 14: DAB converter configuration

The main specifications for the design are input voltage which is equal to the DC output of each CHB sub-module (V_{CHB}), output DC voltage (V_{DAB}), transformer ratio (n_{tr}), leakage inductance (L_{DAB}), switching frequency of DAB (f_s) and DAB output capacitance (C_{DAB}). In the proposed configuration, the output of each DAB creates one charging port, thus the output DC voltage must be the charging voltage requirement of the EV (V_{charg}).

The power of each transformer ($P_{transformer}$) can be calculated as,

$$P_{transformer} = \frac{1}{3} * \frac{P_{rated}}{N} \quad (3.5)$$

The transformer ratio is implemented as the ratio between the input and output voltages at each bridge,

$$n_{tr} = \frac{V_{CHB}}{V_{DAB}} \quad (3.6)$$

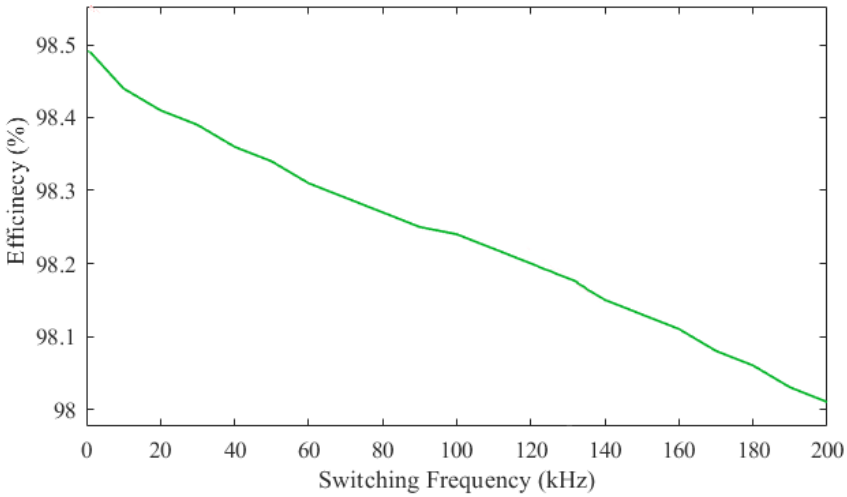

Figure 15: Relationship between the efficiency and switching frequency in DAB converter

The selection of the DAB switching frequency (f_s) requires careful consideration during the design process. Most existing studies commonly adopt a switching frequency of 20 kHz, which is suitable for power ratings ranging from 1 kW to 1 MW [54], [55]. As illustrated in Figure 15, higher switching frequencies result in increased switching losses in semiconductor devices, due to repetitive transitions between ON and OFF states [56]. Lower frequencies, while reducing switching losses, necessitate larger passive components, leading to increased size and weight. A frequency of 20 kHz offers a balanced

trade-off, minimizing both switching losses and the size of passive components like transformers and filters [57].

3.1.3.1 Leakage Inductor

To regulate power flow between the two sides of the transformer, a phase-shift control strategy is employed, which will be discussed in detail later under 3.3.2.1. To support this functionality, an additional inductance is introduced in series with the transformer's leakage inductance. This added inductance, commonly referred to as the leakage inductor, helps limit the current's rate of rise and ensures optimal power transfer [58]. The power flow between the input and output of the DAB converter (P_{DAB}) is expressed as follows.

$$P_{DAB} = \frac{n_{tr} * V_{CHB} * V_{DAB}}{2 * f_s * L_{DAB}} * D_{DAB}(1 - D_{DAB}) \quad (3.7)$$

D_{DAB} refers to the phase shift between the two bridges of the DAB converter. Therefore, the leakage inductance is derived as,

$$L_{DAB} = \frac{n_{tr} * V_{CHB} * V_{DAB}}{2 * f_s * P_{DAB}} * D_{DAB}(1 - D_{DAB}) \quad (3.8)$$

The maximum phase shift (D_{DAB_max}) that can be implemented in the DAB is 0.5. Thus, the minimum leakage inductance is calculated as follows.

$$D_{DAB} \leq 0.5 \quad (3.9)$$

$$L_{DAB} \geq \frac{n_{tr} * V_{CHB} * V_{DAB}}{8 * f_s * P_{DAB}} \quad (3.10)$$

3.1.3.2 HF Transformer

The design of the HF transformer in a DAB converter plays a pivotal role in the overall development of an SST. The transformer's design directly influences the size, weight, and efficiency of the system. The magnetic core's geometric constant, A_P (area product), is a vital factor that determines its ability to handle power and regulate performance effectively. Each core model is defined by a specific A_P value, making its appropriate selection essential in transformer design. In the AP-based design approach for high-frequency, high-power transformers, the A_P value is first calculated to choose a suitable core model [59].

Following this, the transformer's performance parameters are derived based on the core's characteristics and the design specifications.

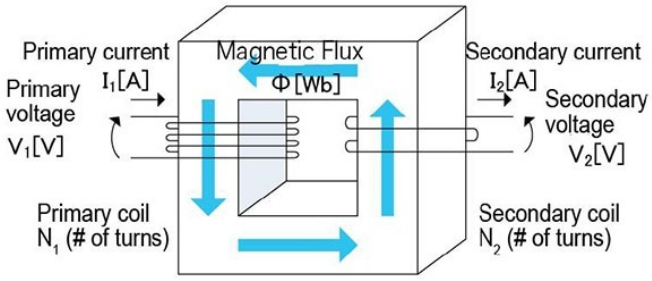

Figure 16: HF Transformer

Let V_1 and V_2 represent the input and output voltages of the transformer, respectively, while $\emptyset$ denotes the magnetic flux within the core. The number of turns in the primary and secondary windings is denoted as n_1 and n_2, as illustrated in Figure 16. Based on these parameters, the following relationships are established [60].

$$V_1 = n_1 \frac{d\emptyset}{dt} \quad (3.11)$$

Considering the flux density is B and the effective cross-sectional area of the core is A_e,

$$B = \frac{\emptyset}{A_e} \quad (3.12)$$

Thus,

$$V_1 = n_1 A_e \frac{dB}{dt} \quad (3.13)$$

$$B = \frac{1}{n_1 A_e} \int V dt \quad (3.14)$$

According to the transformer's hysteresis curve, one of the major considerations is keeping the maximum operating flux density (B_{max}) below its saturation limit ($B_{saturation}$).

$$B_{max} \leq B_{saturation} \quad (3.15)$$

According to the Figure 17,

$$\Delta B = 2B_{max} \quad (3.16)$$

$$\Delta B = 2B_{max} = \frac{V_m t_{on}}{n_1 A_e} \quad (3.17)$$

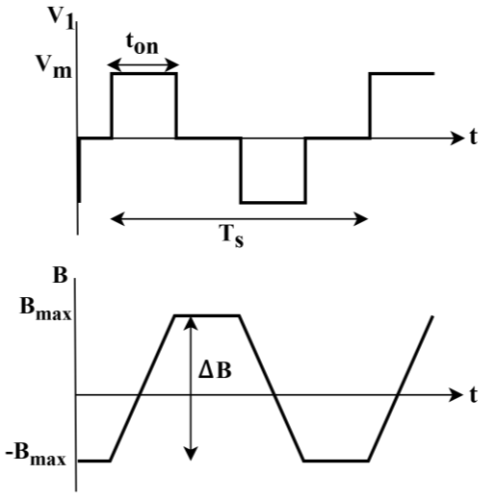

Figure 17: Change of voltage (V) and flux density(B) while switching of the transformer

Thus, the number of turns can be found as,

$$n_1 = \frac{V_m t_{on}}{2B_{max} A_e} \quad (3.18)$$

The windings are wound around the core and the winding window area (A_w) is the total area utilized by the windings in the middle of the core. It can be expressed as a relationship between the number of turns and the cross-sectional area of the winding (W_A) as follows. The k refers to the window utilization coefficient of magnetic core material and (k<=1) [59].

$$A_w = \frac{W_{A1} n_1 + W_{A2} n_2}{k} \quad (3.19)$$

Assuming,

$$W_{A1} n_1 \approx W_{A2} n_2 \quad (3.20)$$

Therefore,

$$A_w = \frac{2W_{A1} n_1}{k} \quad (3.21)$$

$$n_1 = \frac{A_w k}{2W_{A1}} \quad (3.22)$$

From Eq. 3.18 and 3.21,

$$\frac{V_1 t_{on}}{\Delta B. A_e} = \frac{A_w k}{2W_{A1}} \quad (3.23)$$

The area product (A_p) is calculated as,

$$A_p = A_w A_e = \frac{2V_1 t_{on} W_{A1}}{\Delta B. k} \quad (3.24)$$

The winding area, W_A is the ratio between the current passes through the winding (I) and the current density of the winding (J). Also, t_{on} can be expressed as a function of the ON duty time of the PWM (D_{on}) and the switching frequency (f_s)Therefore,

$$A_p = A_w A_e = \frac{2V_1 D_{on} I_{1(rms)}}{\Delta B. k. J. f_s} \quad (3.25)$$

Using Eq. 3.25, the minimum A_p value required for the transformer is determined. Based on the calculated A_p, a suitable core material is chosen. The selection depends on factors such as operating frequency, magnetic saturation flux density, core losses, and thermal stability. The core type (e.g., ferrite, nanocrystalline, or powdered iron) is also selected to align with the application requirements. The A_p value of the selected core must exceed the calculated minimum A_p to ensure that the core can handle the required power without excessive losses or saturation. Then the number of turns is selected using Eq. 3.18.

Transformers used in SSTs require core materials capable of efficient operation at high frequencies while effectively handling substantial power levels. Core materials suitable for this application include ferrite, nanocrystalline, amorphous, and powdered iron. Among these, nanocrystalline cores stand out due to their high saturation magnetic flux density, low core losses, and excellent magnetic permeability [61], [62]. These properties support the development of compact and lightweight electrical devices, offering significant advantages in terms of size, weight, and versatility compared to other core materials. However, the primary drawback of nanocrystalline cores is their relatively high cost. Ferrite cores, on the other hand, are also widely used due to their high magnetic permeability, low losses at high frequencies, lightweight construction, and affordability, making them a practical and cost-effective choice.

Selecting an appropriate winding material for HF transformers is essential to minimize copper losses and eddy current losses, thereby ensuring efficient operation. In most studies, Litz wire is recognized as the preferred choice for high-frequency transformers due to its ability to mitigate the skin effect and significantly reduce eddy current losses at elevated frequencies.[63]. Magnet wires are also employed in certain studies owing to their superior conductivity and cost-effectiveness. However, they tend to exhibit higher losses at very high frequencies, making them less suitable for very HF applications.

3.2 Design of Reconfiguration Algorithm

The reconfiguration algorithm for the EV charging station is designed to dynamically manage switches (S_1 to S_{n-1}) and efficiently allocate charging ports based on the specific requirements of incoming vehicles. The process, illustrated in Figure 18, optimizes the utilization of charging infrastructure by adapting to each vehicle's charging voltage and current needs, which vary depending on battery size and capacity. At the start of the process, all ports (P_1 to P_n) are available, indicated by $P_1=P_2=\ldots=P_n=0$, and all switches (S_1 to S_{n-1}) are in the OFF state, reflected as $S_1=S_2=\cdots=S_{(n-1)}=0$. When a vehicle arrives at the FCS, the algorithm begins by determining whether the vehicle requires high-power charging, which necessitates a series connection. If high-power charging is required, the algorithm checks for the availability of adjacent port pairs sequentially, starting from the top. For instance, it evaluates pairs such as (P_1, P_2), (P_2, P_3),…,($P_{(n-1)}$, P_n). If a pair is vacant (i.e., $P_x=0$ & $P_{x+1}=0$), the vehicle is connected to these ports by activating the corresponding switch S_x, creating a series connection. The status of the ports and switch is then updated to $P_x=P_{x+1}=S_x=1$, indicating that these resources are currently in use. The algorithm continuously monitors the vehicle's charging process until the required State of Charge (SoC) is achieved. Upon completion of charging, the EV is disconnected, and the status of the ports and switch is reset to $P_x=P_{x+1}=S_x=0$, making them available again. If no adjacent port pair is available, the algorithm displays a "No vacancy" message until a pair becomes free.

For vehicles that do not require port reconfiguration, the algorithm prioritizes the use of individual ports. It sequentially checks the availability of each port from top to bottom. If a port P_x is available ($P_x=0$) and the adjacent port P_{x+1} is also free, the algorithm connects

the vehicle to P_x only if all other ports are occupied. This ensures that adjacent ports are reserved for potential high-power configurations. If P_x=0, but P_{x+1}=1, indicating the adjacent port is occupied, the vehicle is still connected to P_x. The algorithm then updates the port status to P_x=1, marking it as occupied. As with high-power charging, the algorithm monitors the vehicle until the desired SoC is reached. After charging, the port status is reset to P_x=0, making it available for future use. In cases where all ports are occupied, the system displays a "No vacancy" message until a port becomes available. This adaptive approach ensures the optimal utilization of charging station resources while accommodating the varying requirements of different EVs, ultimately enhancing the efficiency and flexibility of the charging infrastructure.

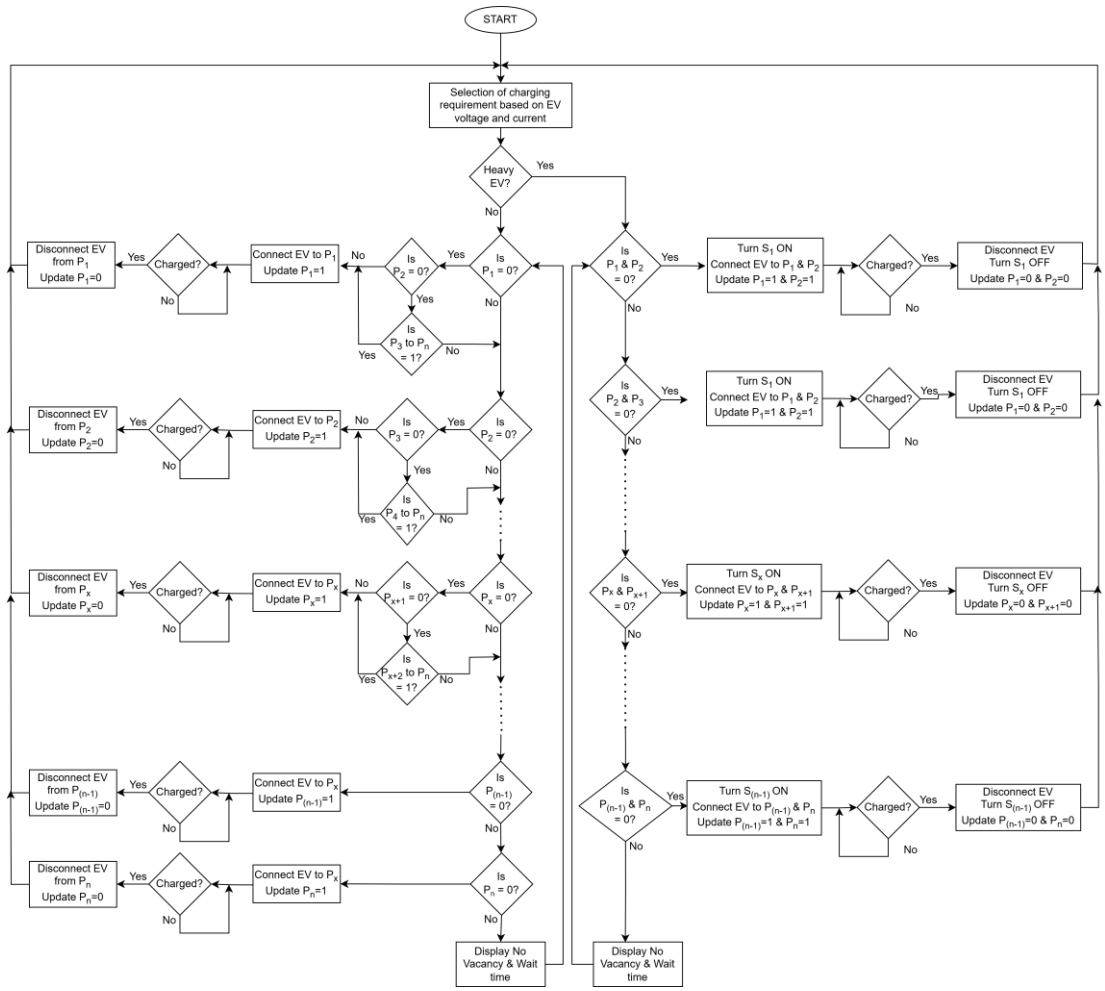

Figure 18: Flow chart of the reconfiguration algorithm

The algorithm is designed to be flexible and can be adjusted to accommodate various EV categories and combinations of output ports, ensuring efficient resource utilization for diverse charging requirements. The flowchart depicted in Figure 18 provides a general framework for configuring charging ports, particularly tailored to handle two distinct EV clusters: Heavy EVs and Medium EVs**.** It systematically evaluates the availability of ports and assigns them in a way that reserves adjacent port pairs for potential high-power configurations needed by Heavy EVs. This prioritization ensures that the charging infrastructure can simultaneously cater to both high-power and low-power EVs without compromising efficiency. By adjusting the algorithm to handle different EV levels and output port configurations, the system achieves enhanced scalability and adaptability. This capability is particularly beneficial for stations that serve a diverse range of EV types, ensuring that all vehicles are accommodated seamlessly while maintaining optimal performance and minimizing downtime.

3.3 Design of the Control System

The main objectives of the control system and the respective controllers can be listed and explained in detail below.

- Regulating a balanced DC voltage at the output of each sub-module of CHB - DC voltage and grid current controller
- Charging the EV according to the Constant Current (CC) charging algorithm - DAB phase shift controller

3.3.1 CHB Voltage Balancing Controller

For the convenience of designing the control system, an average model of the CHB converter is derived first. The average switching function, $\bar{S}(\tau)$ which is also defined as duty cycle (d) can be expressed as,

$$d = \bar{S}(\tau) = \frac{1}{T_s}\int_{t}^{t+T_s} S(\tau)d\tau \qquad (3.26)$$

Therefore, the average input AC voltage ($\bar{V}_{CHB\_AC}$) and the average output current ($\bar{\imath}_{CHB\_DC}$) of a single-phase single module of CHB is derived as,

$$\bar{V}_{CHB\_AC} = \bar{S}(\tau).\bar{V}_{CHB\_DC} = d.\bar{V}_{CHB\_DC} \qquad (3.27)$$

$$\bar{\imath}_{CHB\_DC} = \bar{S}(\tau).\bar{\imath}_{MV} = d.\bar{\imath}_{MV} \quad (3.28)$$

Here, $\bar{V}_{CHB\_DC}$ is the average output DC voltage and $\bar{\imath}_{MV}$ is the average output DC current of a single module of CHB. Using (3.27) and (3.28) the average input AC voltage and average output current of a three-phase n sub-module CHB converter can be derived as follows.

$$\bar{V}_{j\_CHB\_AC} = \sum_{k=1}^{n} d_{CHB\_jk}.\bar{V}_{k\_CHB\_DC} \quad (3.29)$$

$$\bar{\imath}_{jk\_CHB\_DC} = d_{CHB\_jk}.\bar{\imath}_{j\_MV} \quad (3.30)$$

Here, j is denoted for each phase (i.e. j=a,b,c) and k for each sub-module (i.e. k=1,2,…,n). As discussed in the design of the CHB converter, the output voltages and currents of each sub-module of the CHB converter are considered equal and a common duty cycle can be considered for all the sub-modules in each phase. Thus,

$$\sum_{k=1}^{n} d_{CHB\_jk}.\overline{V}_{k\_CHB\_DC} = n.d_{CHB\_j}.V_{CHB\_DC} \quad (3.31)$$

Thus, using Kirchoff's voltage law for the AC side of a single-phase n sub-module CHB converter,

$$n.d_{CHB\_j}.V_{CHB\_DC} + L_{CHB}.\frac{di_{MV\_j}}{dt} - V_{j\_MV\_ph} = 0 \quad (3.32)$$

L_{CHB} is the input filter per phase and V_{j_ph} is the input MV single-phase voltage.

Similarly, considering Kirchoff's current law for the DC side of a single-phase n sub-module CHB converter,

$$d_{CHB\_jk}.\bar{\imath}_{j\_MV} - C_{CHB}\frac{dV_{CHB_{DC}}}{dt} - \frac{V_{CHB_{DC}}}{R_L} = 0 \quad (3.33)$$

R_L is considered as the load at each sub-module. Considering three phases in (3.32) and (3.33) it can be derived,

$$n.V_{CHB\_DC}\begin{bmatrix} d_{CHB\_a} \\ d_{CHB\_b} \\ d_{CHB\_c} \end{bmatrix} + L_{CHB}.\frac{d}{dt}\begin{bmatrix} i_{MV\_a} \\ i_{MV\_b} \\ i_{MV\_c} \end{bmatrix} - \begin{bmatrix} V_{a\_MV\_ph} \\ V_{b\_MV\_ph} \\ V_{c\_MV\_ph} \end{bmatrix} = 0 \quad (3.34)$$

$$[d_{CHB\_ak} \quad d_{CHB\_bk} \quad d_{CHB\_ck}]\begin{bmatrix} i_{MV\_a} \\ i_{MV\_b} \\ i_{MV\_c} \end{bmatrix} - 3C_{CHB}\frac{dV_{CHB_{DC}}}{dt} - \frac{3V_{CHB_{DC}}}{R_L} = 0 \qquad (3.35)$$

As the CHB controller is constructed using Proportional-Integral (PI) controllers, the equations (3.34) and (3.35) are written in the d-q domain using park transformation as below.

$$n.V_{CHB_{DC}}\begin{bmatrix} d_{d_{CHB}} \\ d_{q_{CHB}} \end{bmatrix} + L_{CHB}.\frac{d}{dt}\begin{bmatrix} i_{d_{MV}} \\ i_{q_{MV}} \end{bmatrix} - \begin{bmatrix} 0 & L_{CHB}.\omega_g \\ -L_{CHB}.\omega_g & 0 \end{bmatrix}\begin{bmatrix} i_{d_{MV}} \\ i_{q_{MV}} \end{bmatrix} - \begin{bmatrix} V_{d\_MV\_ph} \\ V_{q\_MV\_ph} \end{bmatrix} = 0 \qquad (3.36)$$

$$[d_{dk\_CHB} \quad d_{qk\_CHB}]\begin{bmatrix} i_{d_{MV}} \\ i_{q_{MV}} \end{bmatrix} - 3C_{CHB}\frac{dV_{CHB_{DC}}}{dt} - \frac{3V_{CHB_{DC}}}{R_L} = 0 \qquad (3.37)$$

Here $\omega_g = 2.\pi.f_g$. To remove time-varying signals variables are given a small perturbation as $x = X + \Delta X$. Then considering only DC terms summarizes into the following equation which is used to control the output DC voltage of each sub-module of the CHB converter.

$$\begin{bmatrix} D_{d_{CHB}} \\ D_{q_{CHB}} \end{bmatrix} = \frac{\begin{bmatrix} 0 & L_{CHB}.\omega_g \\ -L_{CHB}.\omega_g & 0 \end{bmatrix}\begin{bmatrix} i_{d_{MV}} \\ i_{q_{MV}} \end{bmatrix} - \begin{bmatrix} V_{d\_MV\_ph} \\ V_{q\_MV\_ph} \end{bmatrix}}{n.V_{CHB_{DC}}} \qquad (3.38)$$

The block diagram of the CHB controller is shown in Figure 19. Using the Park transformation, the controller transforms the MV grid voltage and current signals into their respective d-q components (V_d, V_q and I_d and I_q). The voltage controller calculates the average output voltage V_{avg_CHB} of the CHB converters and compares it against a predefined reference voltage. Based on this comparison, the controller generates a reference value for the d-axis grid current i_{d_ref}. To achieve power factor correction, i_{q_ref} is set to zero. The controller then compares the i_d and i_q with i_{d_ref} and i_{q_ref}. The resulting error signals are processed by the current controller to produce reference d-q voltage signals (D_d and D_q) which are fed to the pulse width modulation (PWM) switching generator. The PWM generator uses these signals to determine the duty ratios for the switches in the CHB converter.

The controller outputs a common duty ratio (D_{CHB}) that is applied uniformly across all sub-modules. However, since the sub-modules handle varying power levels, this approach results in unbalanced output voltages at the CHB DC outputs, while maintaining the

average output voltage at the desired level. This results in unbalanced voltages across semi-conductor switches.

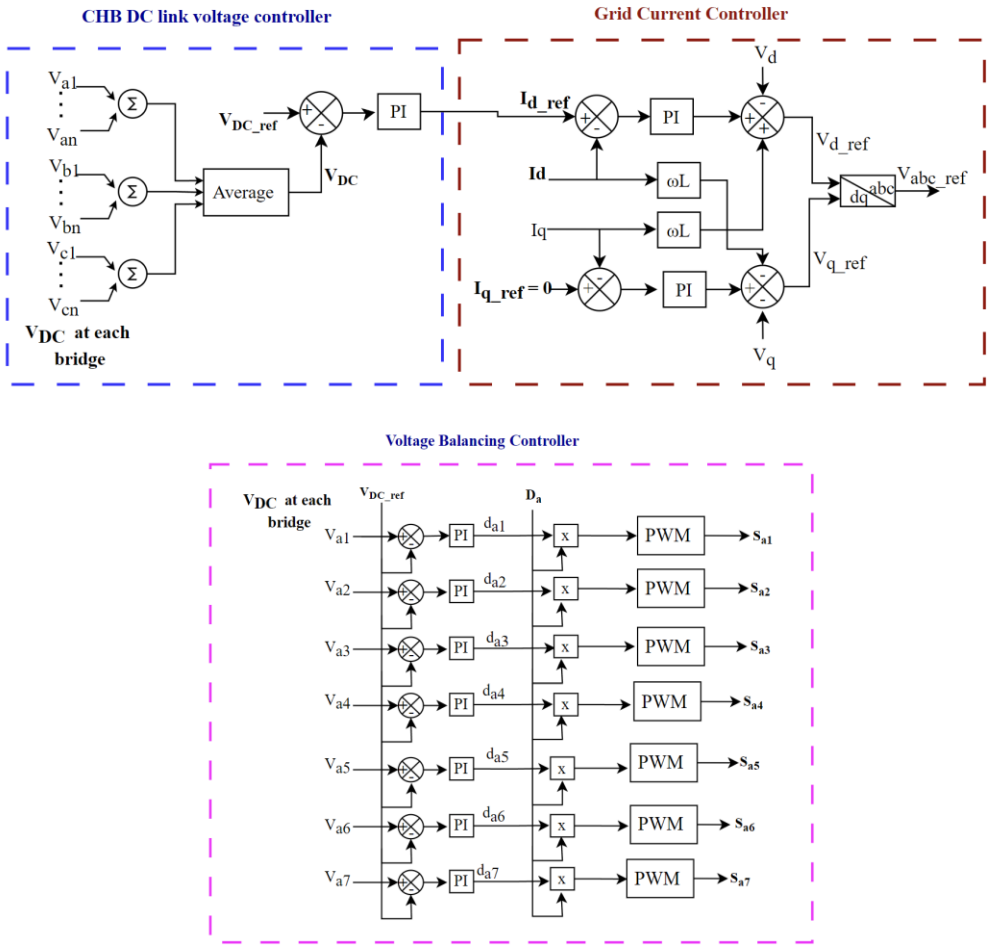

Figure 19: CHB converter voltage balancing controller

To address the issue of voltage imbalance across sub-modules, the proposed control strategy incorporates a corrective addition (d_{CHB}) within the controller. This value is designed to ensure balanced capacitor voltages in each sub-module, enhancing the overall performance of the CHB converter. Unlike conventional methods that apply a uniform duty ratio (D) across all sub-modules, this approach tailors the duty ratio for each sub-module by introducing a dynamic correction factor. Without the balancing controller, the MV AC voltage of single-phase CHB is expressed as (3.39).

$$\bar{V}_{j\_CHB\_AC} = D_{CHB\_j} \sum_{k=1}^{n} . \bar{V}_{k\_CHB\_DC} \quad (3.39)$$

With a corrective addition, it can be expressed as,

$$\bar{V}_{j\_CHB\_AC} = \sum_{k=1}^{n} (D_{CHB\_j} + d_{CHB\_jk}) . \bar{V}_{k\_CHB\_DC} \quad (3.40)$$

Here,

$$\sum_{k=1}^{n} d_{CHB\_jk} = 0 \quad (3.41)$$

As illustrated in Figure 19, the balancing controller continuously monitors the DC output voltage of each sub-module and compares it with the reference voltage. Any detected deviation from the reference value prompts the controller to generate an individual corrective gain (d_{CHB_jk}) and it is generated by a PI controller block. Then d_{CHB_jk} is added to the common duty ratio (D_{CHB_j}) to adjust the switching signals for each sub-module, thereby compensating for voltage discrepancies. The result is a set of optimized duty ratios that align the output voltage of each sub-module with the reference, maintaining uniformity across the entire CHB structure.

3.3.2 DAB Converter Controller

The DAB converter in the proposed system uses phase shift modulation to control power flow by adjusting the phase difference between the pulse-width modulation (PWM) signals of its two bridges. There are four main modulation techniques single phase shift (SPS), extended phase shift (EPS), dual-phase shift (DPS), and triple-phase shift (TPS) modulation [64]. This study analyses mainly SPS and DPS modulation techniques as it is widely used in the state-of-the-art od DAB modulation techniques.

Phase shift modulation is frequently used for the control of DAB as it can achieve Zero Voltage Switching (ZVS). Achieving ZVS in a DAB converter is essential for minimizing switching losses, improving efficiency, and reducing electromagnetic interference (EMI). ZVS occurs when the voltage across the switches becomes zero at the moment of switching. This reduces the power dissipation in the switches and enhances the converter's

overall performance. For better visualization, Figure 20 illustrates the current path of one operation mode of DAB. While the S1 switch turns off the current is forced to flow through the D2 diode due to the inductance of the leakage inductor, L_{DAB} as shown in Figure 21. At this moment the voltage across the S2 switch is nearly zero, thus it can be turned on to achieve ZVS.

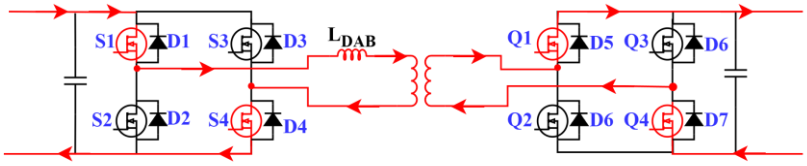

Figure 20: Single mode of operation of DAB converter

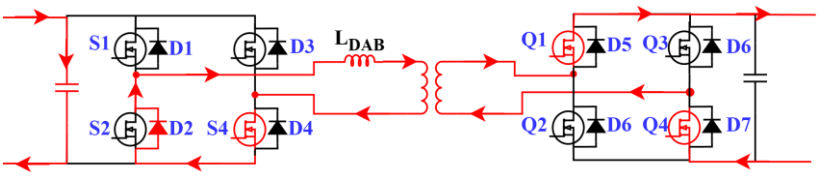

Figure 21: ZVS operation of DAB converter

3.3.2.1 Single Phase Shift

In the SPS modulation method, the phase shift is given only between the corresponding switches of two active bridges having gate signals with a 50% duty cycle as shown in Figure 22 (a). The power flow through the DAB in SPS can be expressed by,

$$P_{DAB\_SPS} = \frac{n_{tr} * V_{CHB} * V_{DAB}}{2 * f_s * L_{DAB}} * D_{DAB}(1 - D_{DAB}) \qquad (3.42)$$

Thus, the voltage present at the transformer terminals is a two-level AC square wave and can be modified by adjusting the phase shift, D_{DAB}. The power going through the converter can be controlled by adjusting the current flowing through the inductor, which is dependent on the voltage across the transformer's terminals. It is simple to perform SPS modulation and accomplish soft switching throughout the operation. However, Zero Voltage Switching (ZVS) cannot be achieved over the whole operational range.

3.3.2.2 Dual Phase Shift

The DPS modulation technique is equipped with two-phase shifts. One is the inner phase shift that exists between the corresponding bridges as in a single-phase shift (D_{DAB_1}) and

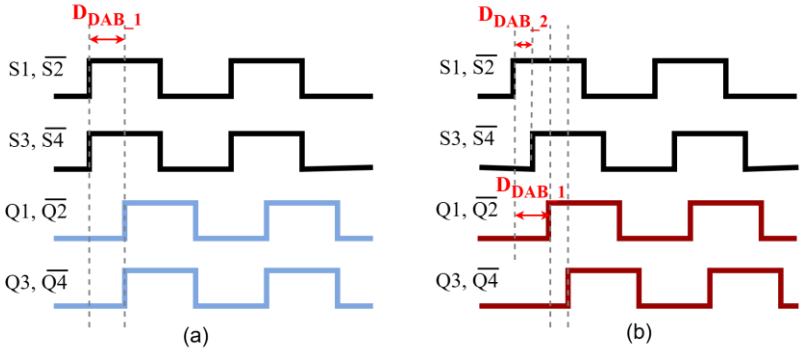

Figure 22: Switching signals for (a) SPS modulation (b) DPS modulation

the other is the inner phase shift (D_{DAB_2}) that exists in between the cross-connected switches in each active bridge which is illustrated in Figure 22 (b). Both sides have the same inner phase shift. The transformer's voltage is in three levels because of the internal phase shift. In contrast, the inner phase shift is reversed to obtain the reverse power flow, increasing the soft-switching range. As a result, the transformer's two sides have a three-level voltage, which increases the ZVS range's efficiency. The power flow through the DAB with DPS can be expressed by,

$$P_{DAB\_DPS} = \frac{n_{tr} * V_{CHB} * V_{DAB}}{2 * f_s * L_{DAB}} * D_{DAB_1}\left(1 - D_{DAB_1}\right) - 2{D_{DAB\_2}}^2 \qquad (3.43)$$

The closed-loop control of the DAB converter relies on an advanced control algorithm to dynamically adjust the phase shift based on system conditions. As depicted in Figure 23, the current controller for the DAB converter includes a current control loop designed to regulate the output DC voltage.

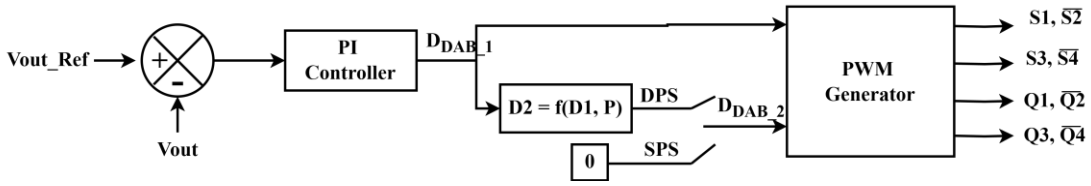

Figure 23: Closed-loop controller of DAB converter

This loop generates the necessary outer phase shift (D_{DAB_1}) by using a PI compensator[65]. The PI compensator ensures the output voltage remains at the desired level by comparing the measured DC voltage with a reference value and adjusting D_{DAB_1} accordingly. The

inner phase shift (D_{DAB_2}) is determined using (3.43), with D_{DAB_2} set to zero for SPS control. The PWM generator then produces the appropriate switching signals based on the values of D_{DAB_1} and D_{DAB_2}. For EV charging, a constant current control algorithm, illustrated in Fig. 23, is employed to maintain a steady and regulated charging current. The controller dynamically computes the required phase shift based on the reference charging current, enabling the DAB converter to efficiently deliver power that meets the variable demands of EVs while ensuring reliable operation.

Chapter 4 Simulation and Experimental Verification

To validate the dynamic performance of the proposed reconfigurable multiport EV FCS, a comprehensive approach combining simulation and experimental validation was adopted which will be described in this chapter.

This chapter aims to demonstrate the feasibility of the proposed system. First, a high-power FCS model is designed and simulated in MATLAB/Simulink. A defined test scenario evaluates the topology's ability to deliver the required voltages and currents to different EVs. Additionally, the feasibility of the reconfiguration algorithm is validated through simulations. The system's impact on the MV grid is assessed by analyzing voltage and current parameters, as well as Total Harmonic Distortion (THD) at the point of common coupling (PCC), particularly during sudden demand changes.

Furthermore, the independent DC bus-based topology has not yet been experimentally validated in the literature. To address this, a small-scale single-phase prototype is developed to verify the concept's practicality for charging multiple EVs. An experimental validation scenario is conducted to evaluate the performance of the balancing and charging controllers. The PCC voltage, current, and THD are also monitored during charging to assess grid interactions.

4.1 Design of 1 MVA EV Fast Charging Station Model for Simulation

Following are the assumptions made for the simulation model.

- The components are ideal and lossless.
- The HF transformer is assumed to be perfectly magnetically coupled.
- Constant load and source conditions are assumed with no disturbances from the grid.
- Thermal effects are neglected.

4.1.1 Simulation Parameters

To assess the performance of the proposed system under varying demand conditions, a MATLAB/Simulink model was developed. This study considers three EV categories;

heavy, medium, and light each with distinct charging current and nominal voltage requirements. The system is designed to support three distinct EV categories:

- Heavy EV (buses, trucks)- 150 kWh, 800 V battery (i.e. Ford F-150 Lightning)
- Medium EV (cars) - 50 kWh, 400 V battery (i.e. Tesla Model 2)
- Light EV (three and two-wheelers) - 10 kWh, 200 V battery (i.e. Renault Twizy)

The simulation parameters for the proposed reconfigurable multiport EV FCS are outlined in Table 2.

Table 2: Simulation model parameters for proposed EV FCS

Parameter Name	**Value**
SST Parameters	
Grid voltage ($V_{g\ -a,b,c}$)	11 kV_{L-L}
Grid frequency (f_g)	60 Hz
Power rating (P)	1 MVA
CHB sub-module DC output (V_{CHB_DC})	1.2 kV
No. of submodules per phase (n_{CHB})	7
Input filter (L_a, L_b, L_c)	20 mH
CHB Output Capacitor (C_{CHB})	1.5 mF
DAB leakage inductance (L_{DAB})	16.5 µH
DAB switching frequency (f_s)	20 kHz
DAB output capacitor (C_{DAB})	0.9 mF
Heavy EV	
Nominal Battery Voltage (V_H)	800 V
Battery Capacities (E_H)	150 kWh
Charging current references (I_H)	375 A
Medium EV	
Nominal Battery Voltage (V_M)	400 V
Battery Capacities (E_M)	50 kWh
Charging current references (I_M)	250 A
Light EV	
Nominal Battery Voltage (V_L)	200 V
Battery Capacities (E_L)	10 kWh
Charging current references (I_L)	100 A

The design incorporates a reconfigurable structure with multiple DC buses enabled by an SST to meet the requirements of EV fast charging as illustrated in Figure 24.

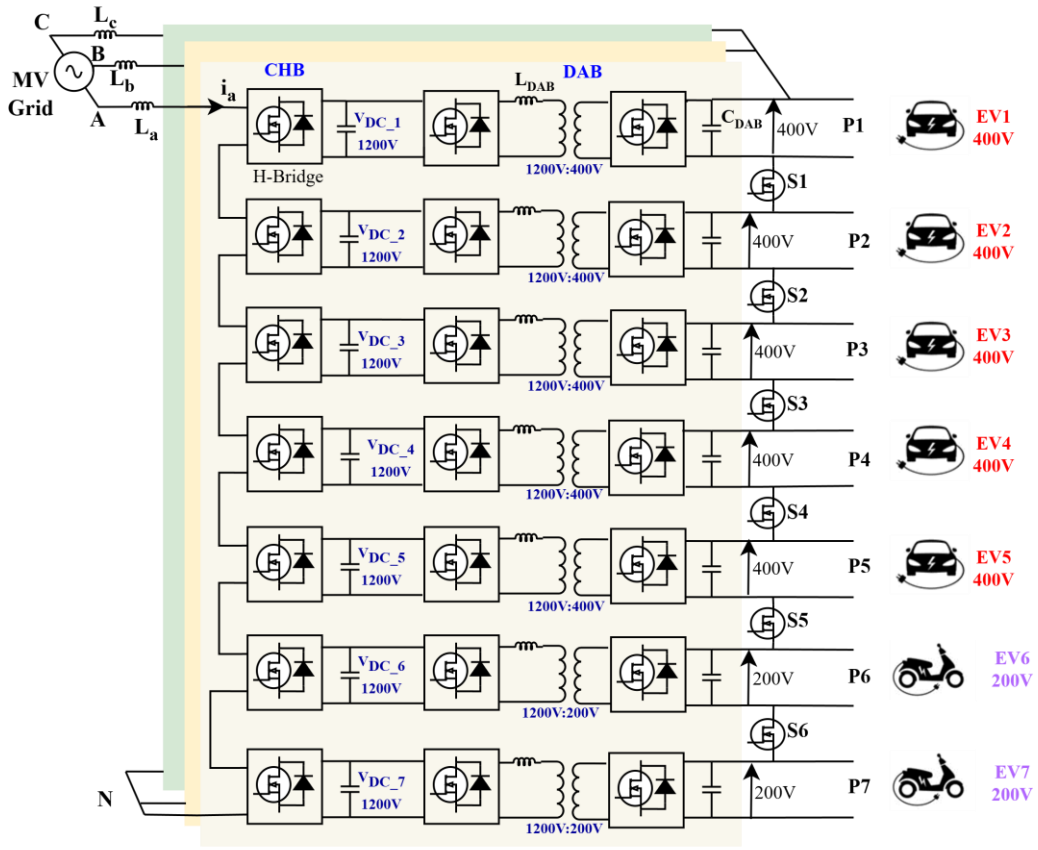

Figure 24: Proposed DC FCS model used in simulation

Key specifications considered for the design are as follows:

- Rated Power: 1 MVA
- MV Grid: 11 kV, 60 Hz

To implement the system, CREE C2M0025120D Silicon Carbide (SiC) MOSFETs are considered, which have rated voltage and current ratings of 1200 V and 39 A, respectively. The output voltage for each sub-module of the CHB converter is set to 1200 V. Based on this, the number of CHB sub-modules per phase (n_{CHB}) is calculated as 7, using equation (3.2). The DAB converter output voltage is designed to match the range of EV battery voltages. The first five DABs are configured to provide output ports with 400V, while the remaining two DABs are designed for 200 V outputs. This modular design allows for

flexibility in achieving the required charging voltages where two 400 V ports can be connected in series to create an 800 V port. Similarly, two 200V ports can be connected in series to form a 400 V port. To facilitate these configurations, the HF transformers within the DAB con200V for the 200 V outputs. The switching frequency of the DAB converter is selected as 20kHz and the leakage inductance is calculated to be 16.5 μH. Figure 25 illustrates the various configurations of the EV charging ports, showcasing how the system achieves the desired charging voltage and current levels through its modular and reconfigurable design. This approach ensures compatibility with diverse EV battery specifications, enhancing the station's flexibility and efficiency.

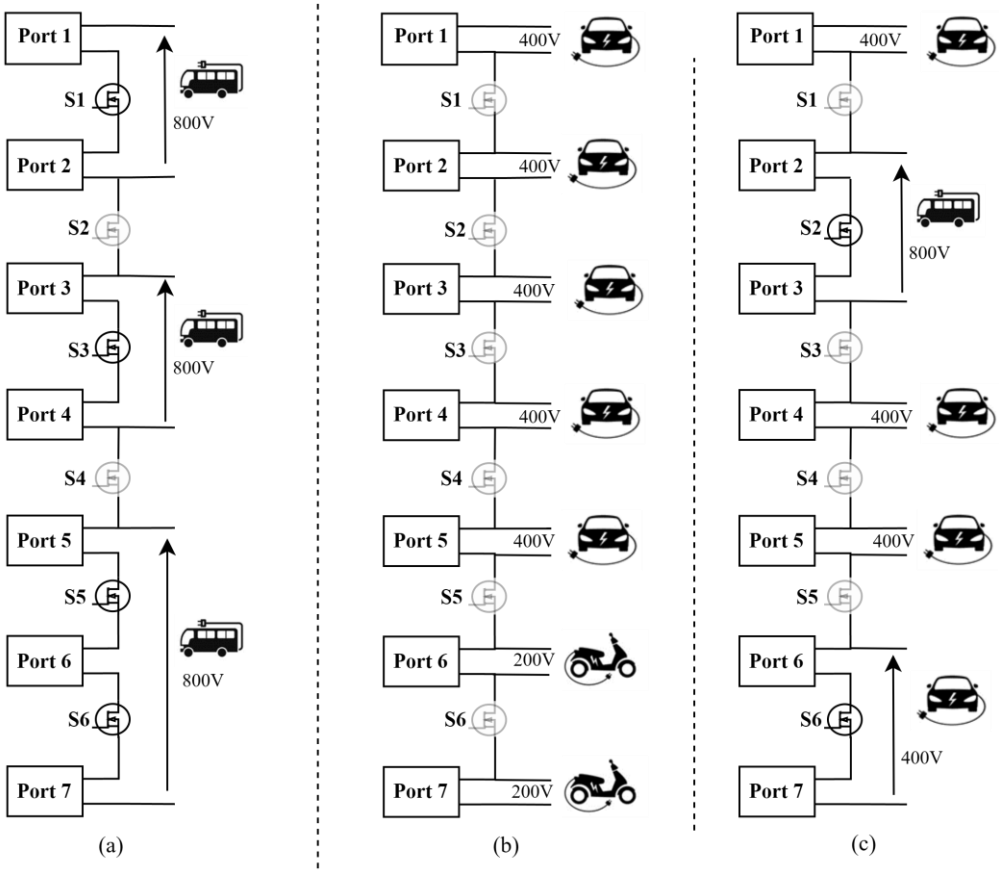

Figure 25: Three possible configurations of S1 to S6 catering different EVs (a) Three 800V ports (b) Five 400V ports and two 200V ports (c) Four 400V ports and one 800V port

4.1.2 Simulation Scenarios

To validate the dynamic behavior of the charging station and evaluate the effectiveness of the reconfiguration algorithm, a predefined scenario as illustrated in Figure 26 and explained below was simulated using the developed model in MATLAB/Simulink. This

study considers three EV categories; heavy, medium, and light each with distinct charging current and nominal voltage requirements.

- From (0-1) s - Two heavy EVs (EV1, EV2) are connected to ports P_1-P_2 and port P_3-P_4 respectively. One medium EV (EV5) is connected to port P_5. Two light EVs (EV6, and EV7) are connected to ports P_6 and P_7 respectively.
- From (1-2) s - EV1(a heavy EV) leaves the charging station vacating port $P_1$and P_2. As EV1 departs, the S1 switch is opened. The remaining vehicles continue charging at their respective ports.
- From (2-3) s - A medium EV (EV3) arrives at the charging station and is assigned to port P_1 as determined by the reconfiguration algorithm.
- After 3 s - Another medium EV (EV4) arrives at the charging station and is connected to port P_2 following the recommendation of the reconfiguration algorithm.

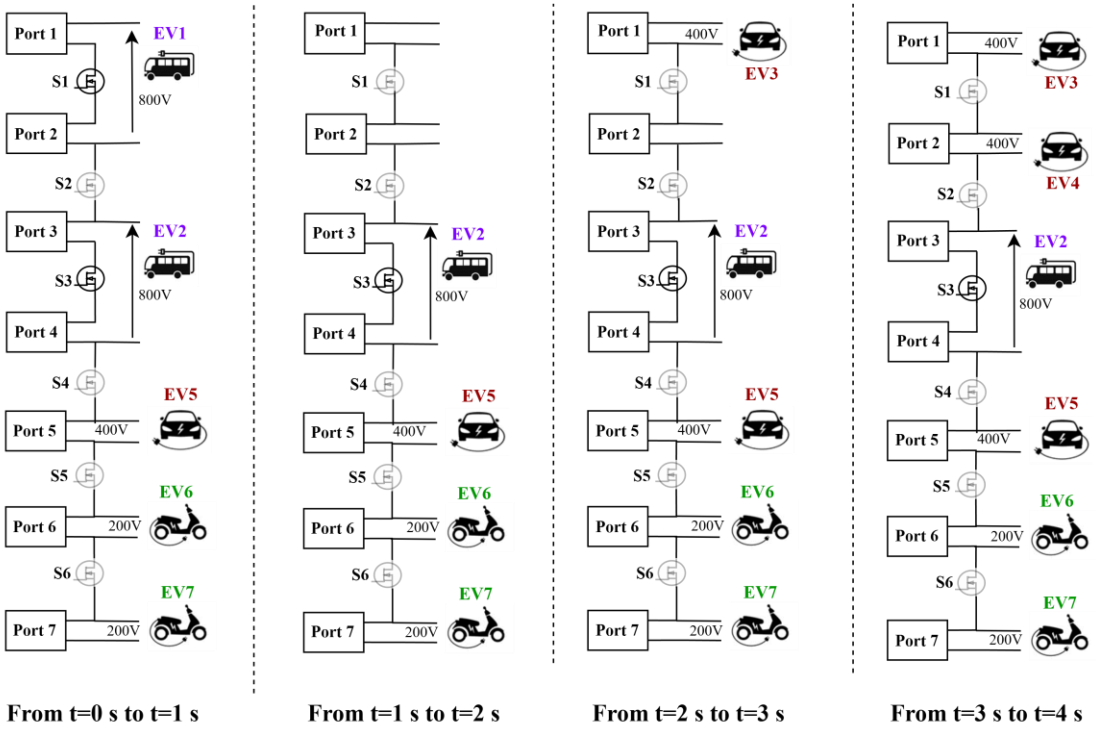

Figure 26: Simulation scenario with dynamic load changes

This scenario demonstrates the algorithm's ability to dynamically reconfigure the charging station's resources to efficiently accommodate varying vehicle arrivals and departures. The simulation setup and corresponding results are outlined in the following section.

4.2 Simulation Results

This section presents the simulation results, divided into two distinct parts to verify the performance and functionality of key components of the proposed system:

- CHB DC output voltage balancing controller
- Reconfiguration algorithm

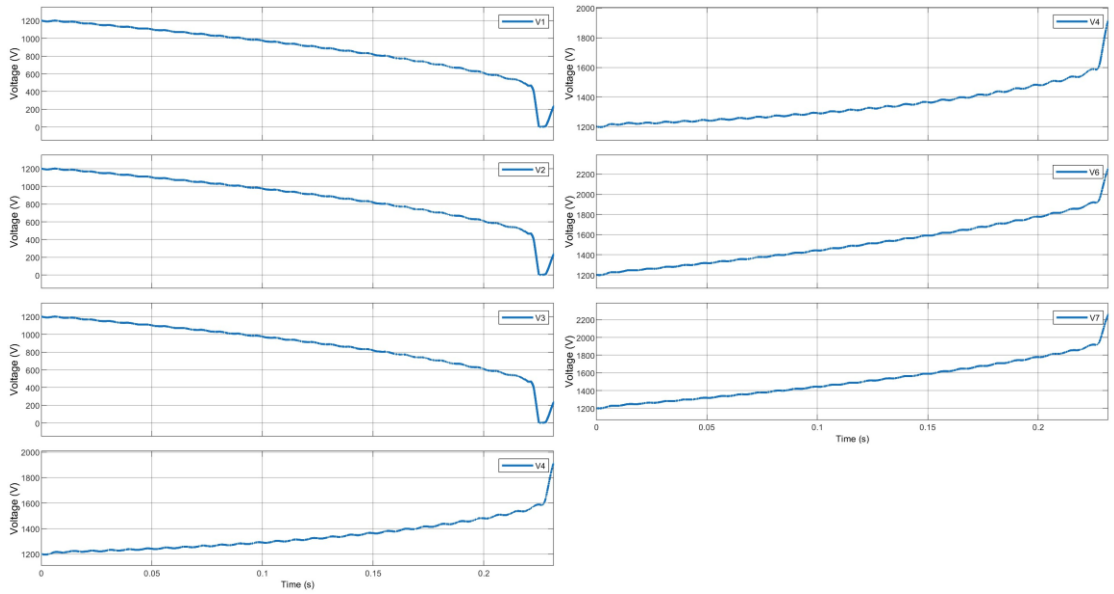

Figure 27: DC output voltage at each sub-module of CHB (from 1 to 7) without the balancing controller

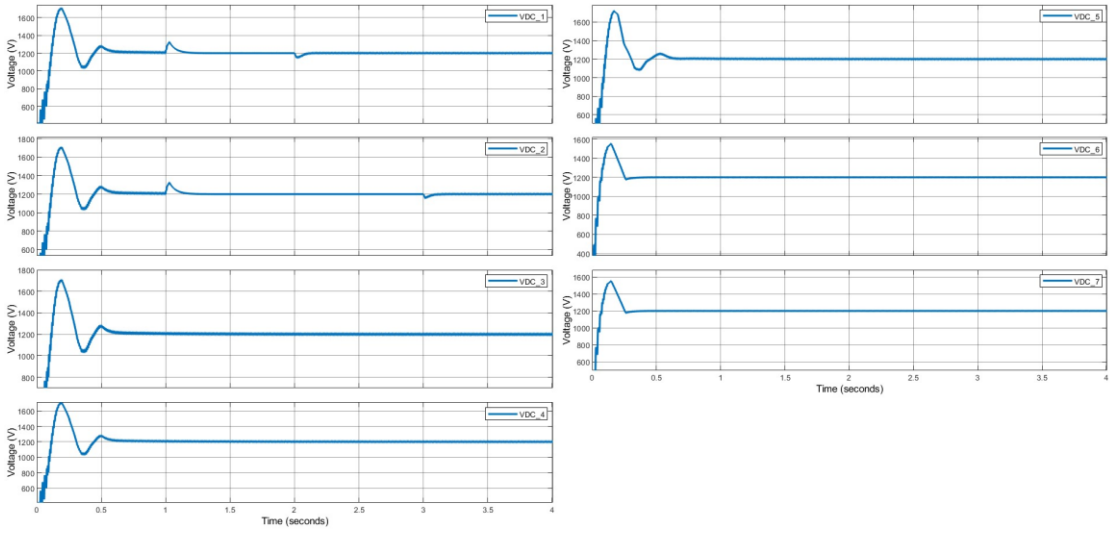

Figure 28: DC output voltage at each sub-module of CHB (from 1 to 7) with the balancing controller

4.2.1 CHB Controller Simulation Results

The verification of the CHB controller focuses on assessing its performance in generating balanced output voltages across all submodules under dynamic load conditions. Simulations were conducted under the scenario described in Section 4.1.2, both with and without the balancing controller. The output DC voltages at each CHB submodule are illustrated in Figure 27 and Figure 28.

Figure 27 shows the results without the balancing controller, where significant voltage instability is observed. In this case, the output voltages are unbalanced due to varying power draws from each submodule, leading to voltage collapse. Conversely, Figure 28 presents the simulation results with the balancing controller implemented. The balancing controller effectively maintains a stable output voltage of 1200 V per submodule, ensuring synchronization and voltage balance across all phases. Furthermore, the controller demonstrates robustness in the presence of dynamic load changes at t=1 s, t=2 s, and t=3 s, consistently regulating the output voltage at the desired level of 1200 V. These results confirm the controller's fast response time, high accuracy in addressing disturbances, and overall reliability and effectiveness in maintaining voltage stability, even under varying operating conditions.

4.2.2 Reconfiguration Scenarios

Figure 29 and Figure 30 show each vehicle's charging current and voltage profiles respectively as they arrive at the DC fast charging station. Based on the simulation scenario described earlier, the initial charging currents for EV1, EV4, EV5, EV6, and EV7 are 375A, 375A, 250A, 100A, and 100A, respectively as observed in Figure 29.

At t=1 s, EV1 departs the charging station, vacating its assigned port. Subsequently, at t=2 s, EV2 arrives and is assigned to port P_1 where it starts charging at 250A, as shown in Figure 29. At t=3 s, EV3 arrives at the charging station and started charging at 250A current via port P_2. In addition to the current profiles, the voltage profiles of the EV batteries at their respective ports are shown in Figure 30. The battery voltages increase steadily as the

vehicles are charged, reflecting the effective operation of the reconfiguration algorithm in maintaining optimal charging conditions for each vehicle.

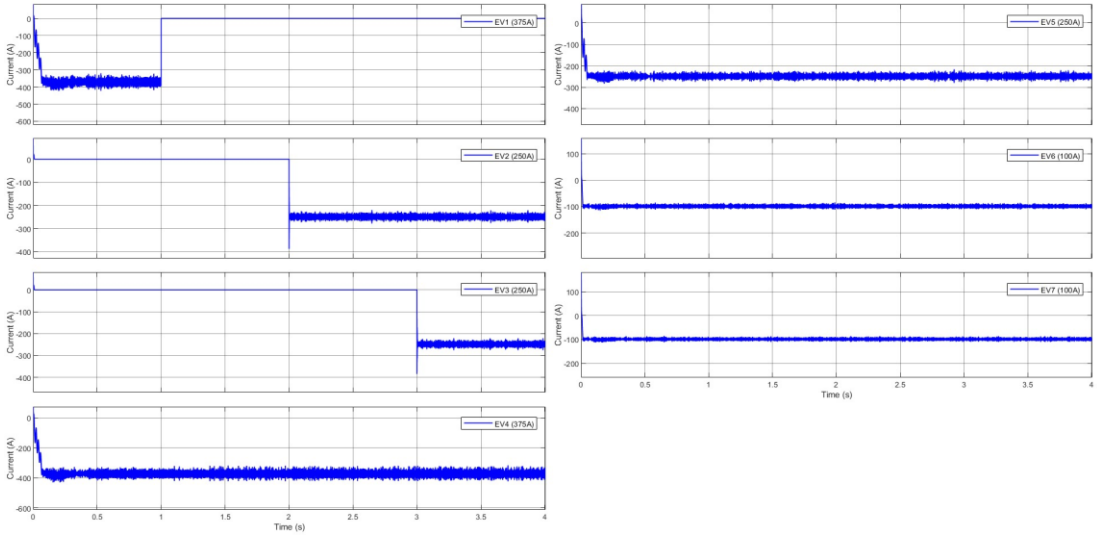

Figure 29: Charging current profiles of EVs according to the simulation scenario

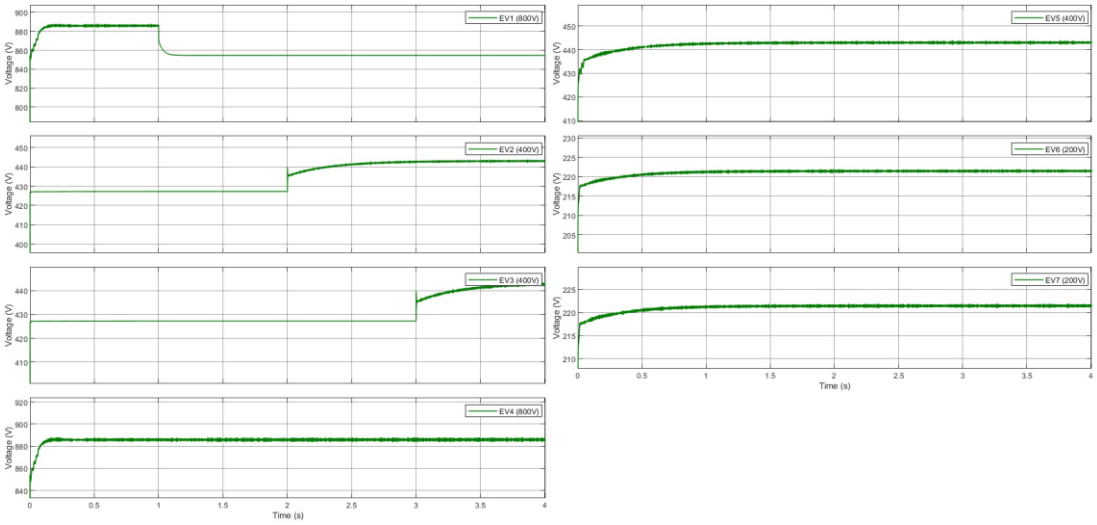

Figure 30: Charging voltage profiles of EVs according to the simulation scenario

4.2.3 Grid Behavior

Figure 31 presents the grid voltage and current waveforms for the simulation scenario. It is observed that despite disturbances occurring at t=1 s, t=2 s, and t=3 s, the grid voltage and current maintain stability throughout the simulation. Additionally, the average output DC

voltages of the CHB sub-modules in each phase are effectively regulated at 1200V, as shown in Figure 31.

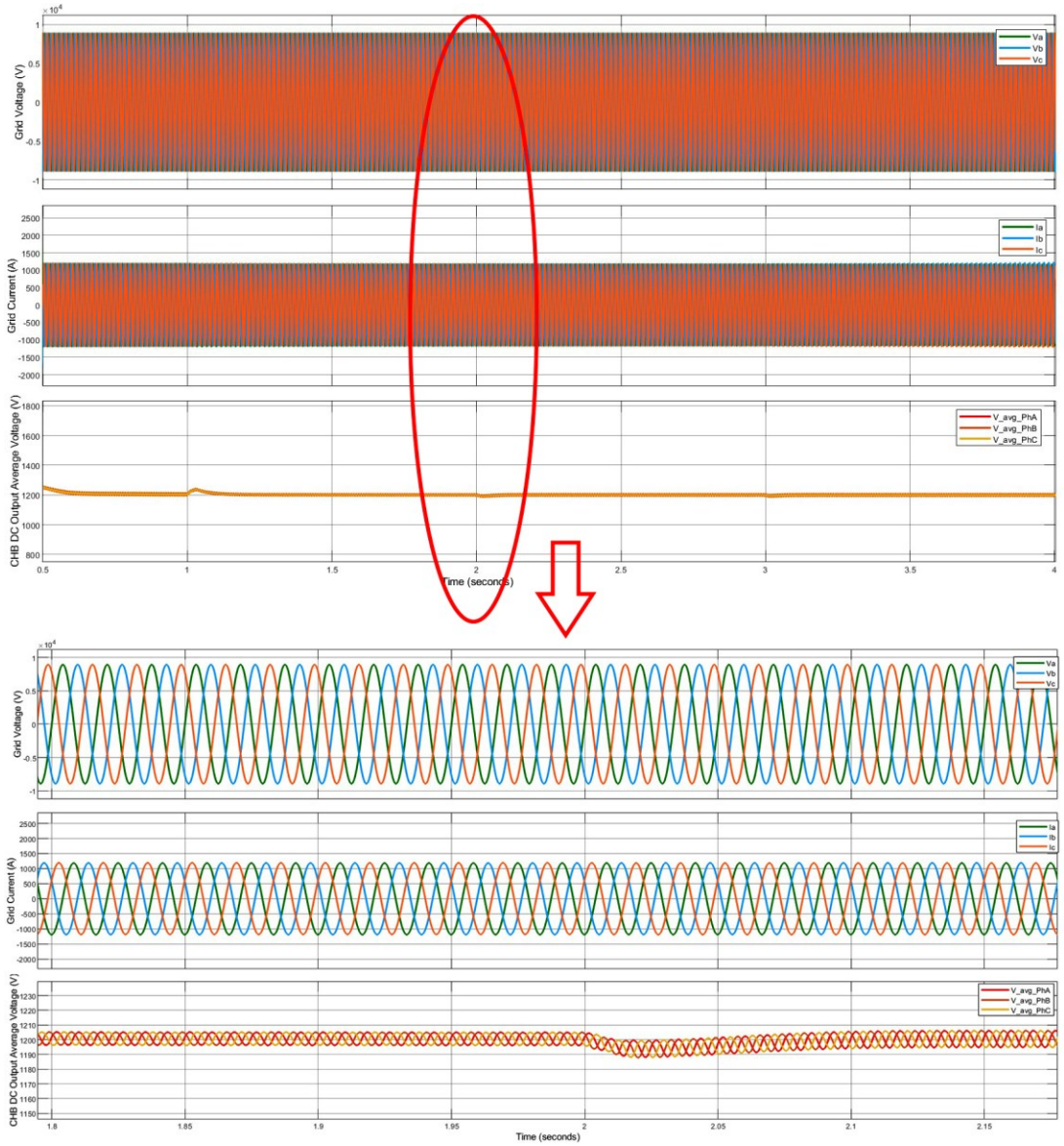

Figure 31: Grid voltage, grid current and average output DC voltage of CHB at each phase

Furthermore, the total harmonic distortion (THD) of the grid current is kept below 5%, as depicted in Figure 32. This THD level complies with the IEEE 519-2022 standard, demonstrating the system's capability to ensure harmonic distortion remains within acceptable limits under varying operational conditions.

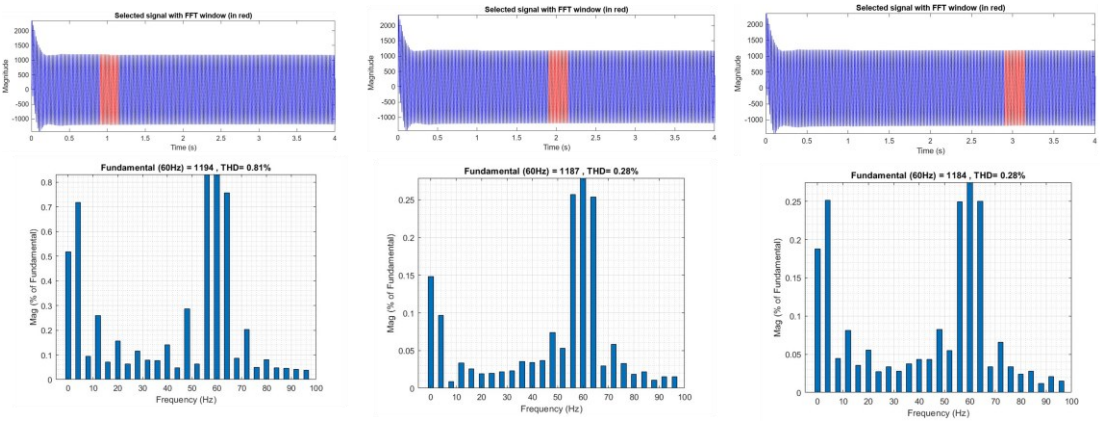

Figure 32: THD of grid current waveform after the demand changes

4.3 Experimental Validation

The experimental validation of the proposed EV fast charging station is conducted using a scaled-down prototype featuring a single-phase, three-level DC fast charging configuration. The primary objective of this setup is to verify the feasibility of the proposed topology. While the simulation is performed for a 1 MVA, 11 kV three-phase charging station to reflect real-world applications, the experimental prototype is developed as a 3.3 kW single-phase system. This setup accommodates two categories of EVs, considering practical limitations within the laboratory environment. Since the proposed system is scalable to match any power level by changing the number of sub-modules, this is experimentally validated after scaling-down to 3.3 kW.

4.3.1 Experimental Parameters

The experimental setup specifications are provided in Table 3, and the prototype is shown in Figure 33.

Table 3: Specification of the experimental prototype

Parameter Name	**Value**
SST Parameters	
Grid voltage ($V_{g\text{-}ph}$)	108 V_{L-L}
Grid frequency (f_g)	60 Hz
Power rating (P)	3.3 kW
CHB sub-module DC output (V_{CHB_DC})	50 V

No. of submodules (n_{CHB})	3
Input filter (L_a)	10 mH
CHB Output Capacitor (C_{CHB})	3300 µF
DAB leakage inductance (L_{DAB})	6.5 µH
DAB switching frequency (f_s)	20 kHz
DAB output capacitor (C_{DAB})	230 µF
Heavy EV	
Nominal Battery Voltage (V_H)	100V
Charging current references (I_H)	2.5 A
Light EV	
Nominal Battery Voltage (V_M)	50V
Charging current references (I_M)	1.25 A

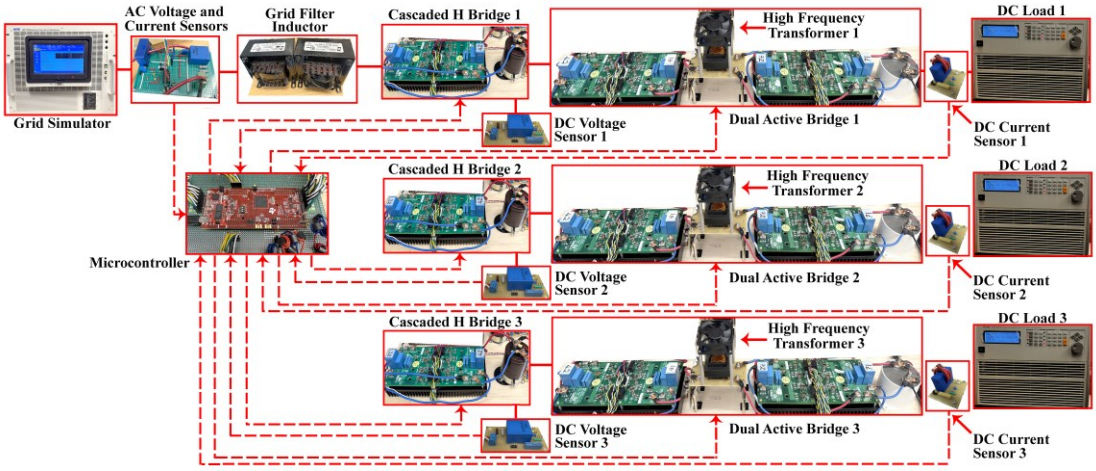

Figure 33: 3.3 kW prototype of single-phase 3 level EV FCS proposed by the study

Designed with a capacity of 3.3 kW, the experimental system operates on a single-phase configuration to demonstrate the charging algorithm, despite the simulation being performed for a three-phase system. The setup is powered by a 108V, 60Hz single-phase grid supply due to the practical limitations of lab testing. For this validation, two categories of EVs are considered: a heavy EV with a charging port of 100V, 2.5A, and a light EV with a charging port of 50V, 1.25A. The CHB converter consists of three levels, with each module output regulated to 50V DC. The DAB converter, connected to each CHB submodule, utilizes high-frequency transformers with a 1:1 turns ratio and operates at a switching frequency of 20 kHz.

The front-end CHB converter is implemented using CREE 8FF1217P-1 MOSFET evaluation modules, which are equipped with CREE C2M0080120D SiC MOSFETs. Voltage and current measurements are captured using LV 20-P and LA 55-P transducers respectively. Additionally, the TMS F28379D launchpad is employed to implement the feedback controllers for both the CHB and DAB converters, ensuring precise control and validating the system's performance.

4.3.2 Validation Scenarios

The prototype is experimentally tested under two reconfiguration scenarios to validate its performance:
Scenario 1 - Three light EVs are charged at each port, with each providing 1.25A at 50V.
Scenario 2 - One heavy EV is charged by series-connecting ports P_1 and P_2, delivering 2.5A at 100V, while one light EV at port 3, provides 1.25A at 50V.

The constant current charging algorithm is implemented within the DAB controller to maintain a regulated charging current at the output. To simulate real-world battery behavior under controlled laboratory conditions, DC electronic loads are used during the experiment.

4.4 Experimental Validation

This section describes the design of the experimental setup and the validation of its performance.

4.4.1 CHB Converter Experimental Validation

The prototype of the CHB converter is designed as a single-phase, 3-level system. The primary objective of the controller in this prototype is to regulate the DC voltage output of each submodule to a predefined voltage set point. For the design of the prototype, a single-phase 108V grid supply is considered referring to the single-phase power supply ratings in Canada. As there are three sub-modules (n_{CHB}=3) and considering the equation (3.2), the output DC voltage (V_{CHB_DC}) is selected as 50V. As depicted in Figure 34, the output DC voltage of all three submodules remains well-regulated at 50 V, despite variations in the power extracted from each submodule. This consistent voltage regulation across submodules demonstrates the effectiveness of the balancing controller implementation. The results validate the controller’s ability to maintain voltage stability under uneven

power distribution conditions, ensuring the reliable operation of the CHB converter prototype.

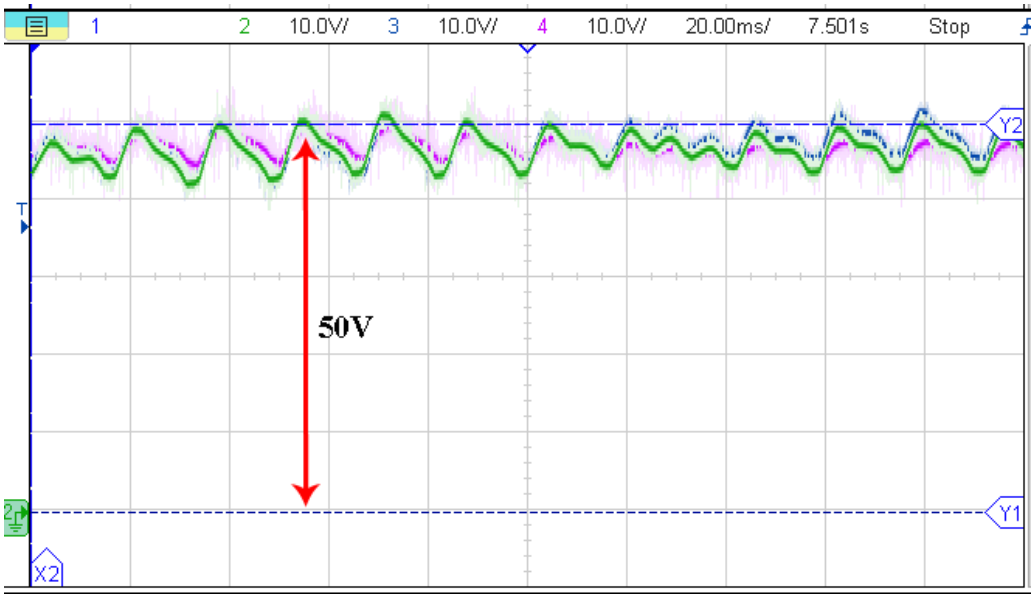

Figure 34: Balanced DC output voltages of the three sub-modules of CHB converter

4.4.2 DAB Controller Experimental Validation

The experimental prototype uses three DAB converters connected at the output of each sub-module of the CHB. For the primary and secondary bridges of the DAB converter, CREE 8FF1217P-1 MOSFET evaluation modules, which are equipped with CREE C2M0080120D SiC MOSFETs are used. The transformer design is explained below.

4.4.2.1 HF Transformer Experimental Validation

Although nanocrystalline material is often the most suitable core material for transformers due to its availability and cost-effectiveness, the prototype employs Ferrite E C394 material with an EE core shape (E42/2115-3C94 core). The transformer in this design is rated for 1.1 kW, with input and output voltages both designed to be 200 V, corresponding to a 1:1 transformer ratio. The maximum current rating is specified as 5.5 A. The windings are constructed using AWG 16 magnet wire, selected for its better conductivity at high frequencies. The number of primary and secondary turns is determined using Equation (3.18), considering the design parameters and core material characteristics. The maximum

flux density is set at 0.4 T to ensure the transformer operates within a safe thermal limit, corresponding to a maximum power dissipation of 100 mW/cm³ as indicated in the core material's datasheet. Based on these considerations and the calculations from Equation (3.18), the required number of turns for both the primary and secondary windings is determined to be 30. This design ensures the transformer achieves optimal performance while adhering to thermal and electrical constraints.

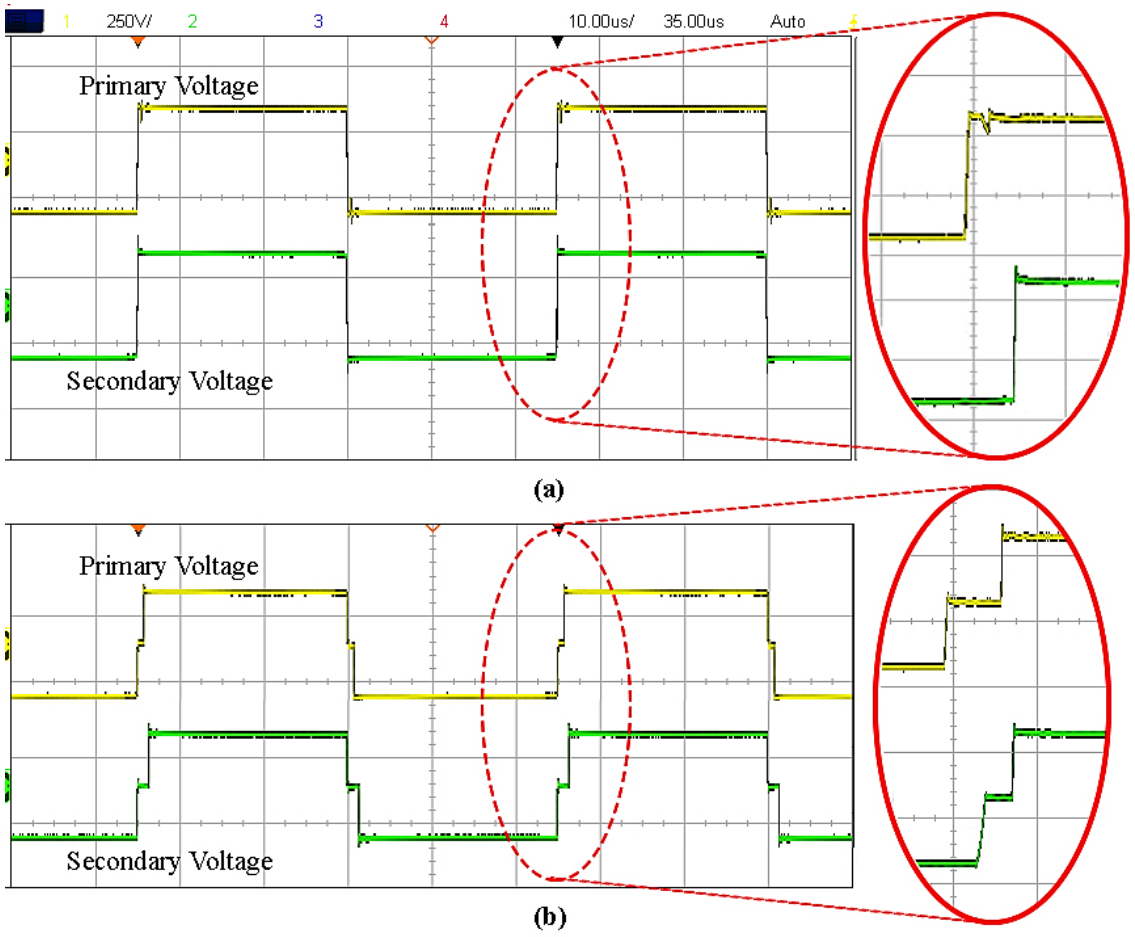

Figure 35: Transformer primary and secondary voltages with (a) SPS and (b) DPS modulation

The transformer performance was experimentally validated with the closed-loop control for SPS and DPS modulation. Figure 35 illustrates the primary and secondary voltages of the transformer for SPS and DPS modulation. The voltage is a two-level waveform in SPS and a three-level waveform in DPS modulation. This is due to the inner phase shift introduced in the DPS modulation technique. Figure 36 depicts the drain-to-source voltage

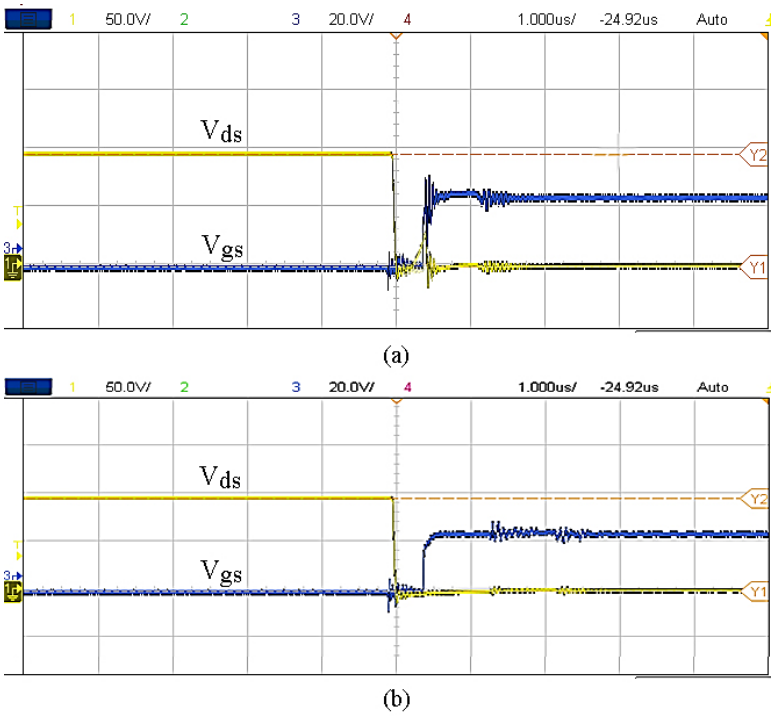

Figure 36: Drain-to-Source (Vds) and Gate-to-Source (Vgs) voltages of a single switch for (a) SPS and (DPS) modulation

(V_{ds}) and gate-to-source (V_{gs}) voltage of a single switch which implies the ZVS phenomena in both SPS and DPS modulation. It can be observed that the V_{ds} is zero before the gate signal is applied to the switch which means at the time of turn-on, the diode was conducting, therefore, the voltage across the switch happened to be zero at the time of

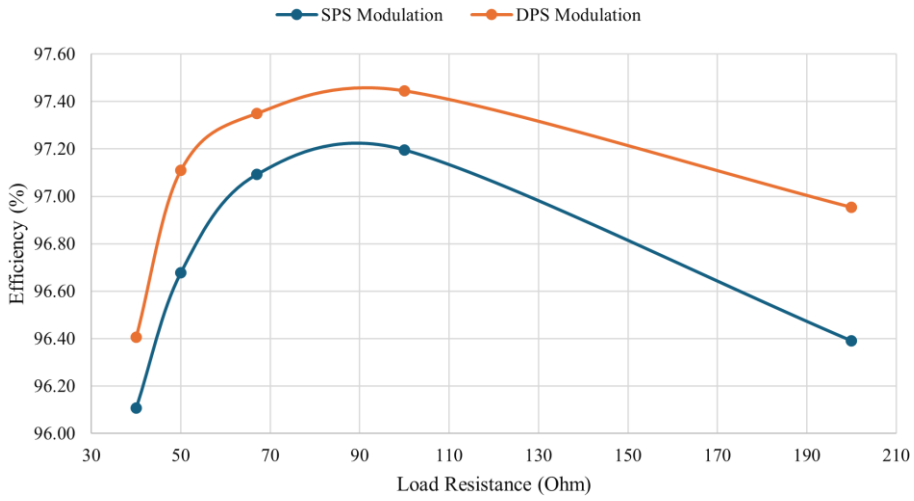

Figure 37: Efficiency of the DAB prototype for SPS and DPS modulation under different load conditions

switching for both modulation conditions. In addition, the efficiency of the hardware model for SPS modulation and DPS modulation was observed for different load conditions and the results are depicted by the graph shown in Figure 37. The load resistance was changed from 200Ω to 40Ω, such that the load power changes from 0.2kW to 1kW. However, the efficiency of the system with DPS modulation, was always higher than that of SPS modulation. The average efficiency for SPS and DPS modulation techniques were observed to be 96.69% and 97.05% respectively.

4.4.3 Reconfiguration Scenarios

As detailed in Section 4.3.2, the simulation results are presented for two charging scenarios. In the first scenario, three light EVs are charged simultaneously, each drawing 1.25 A per port. The voltage at each port is regulated to 50 V, as shown in Figure 38, while the current profile for each port is illustrated in Figure 39. This configuration delivers a total power

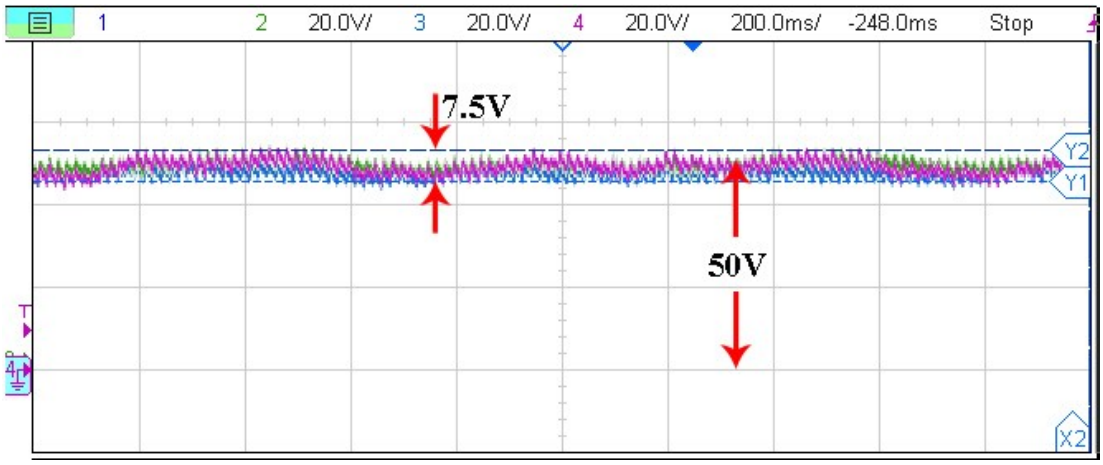

Figure 38: DC output voltage at each port in scenario 1

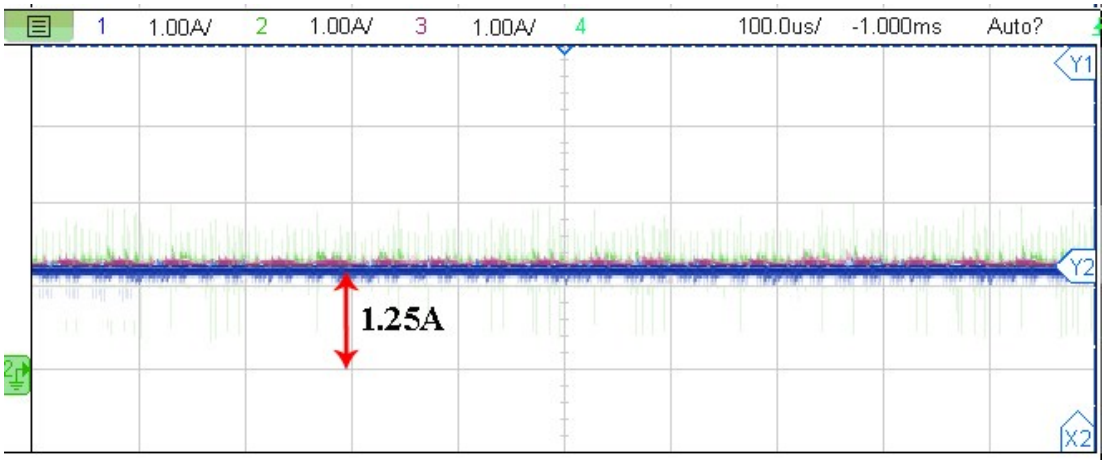

Figure 39: DC output current at each port in scenario 1

output of 187.5 VA. The observed peak-to-peak voltage ripple is 15%, demonstrating stable performance under light-load conditions.

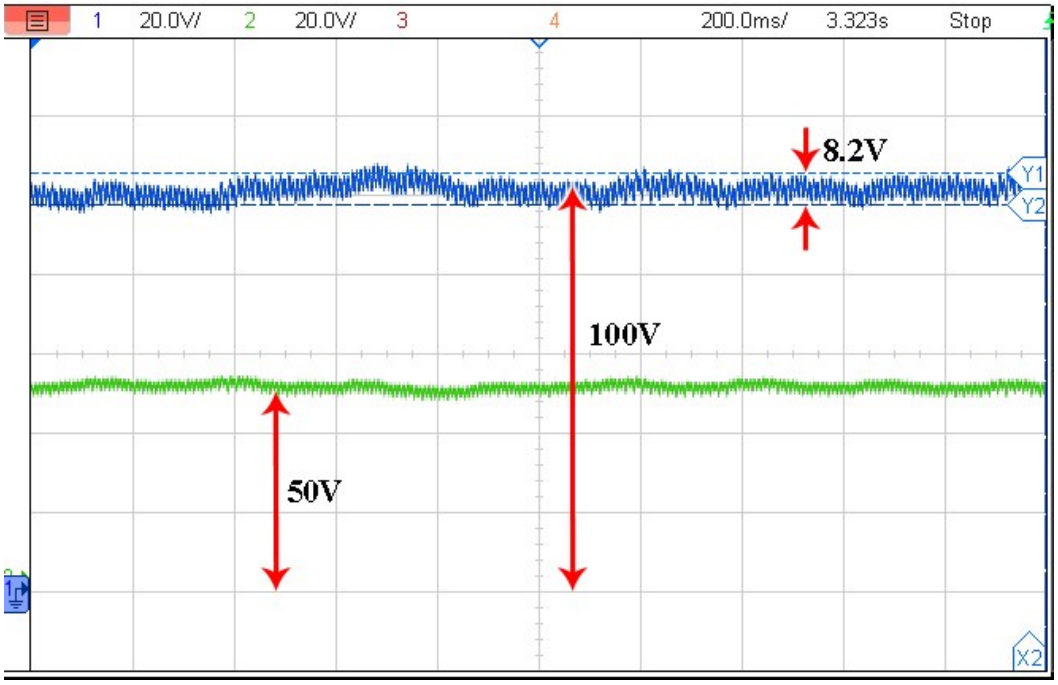

Figure 40: DC output voltages at each port in scenario 2

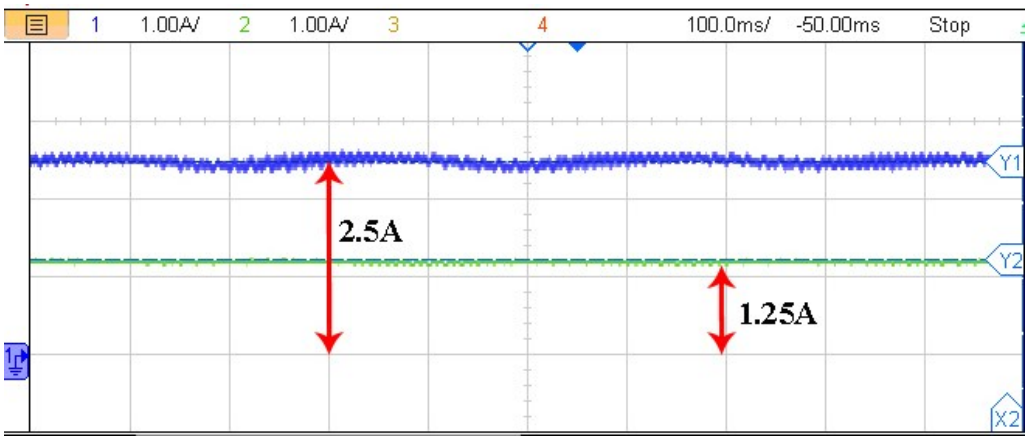

Figure 41: DC output currents at each port in scenario 2

In the second scenario, one heavy EV is charged at 2.5 A by series-connecting Ports 1 and 2, while one light EV is charged at 1.25 A via Port 3. The voltage distribution is depicted in Figure 40, where the heavy EV receives 100 V from the series connection, and the light EV receives 50 V. Correspondingly, Figure 41 shows the current distribution, with the heavy EV receiving 2.5 A and the light EV receiving 1.25 A. This setup delivers a combined power output of 312.5 VA. The peak-to-peak voltage ripple is reduced to 8.2%,

highlighting improved stability under mixed-load conditions. These results validate the system's ability to regulate voltage and current effectively while dynamically adapting to diverse charging requirements.

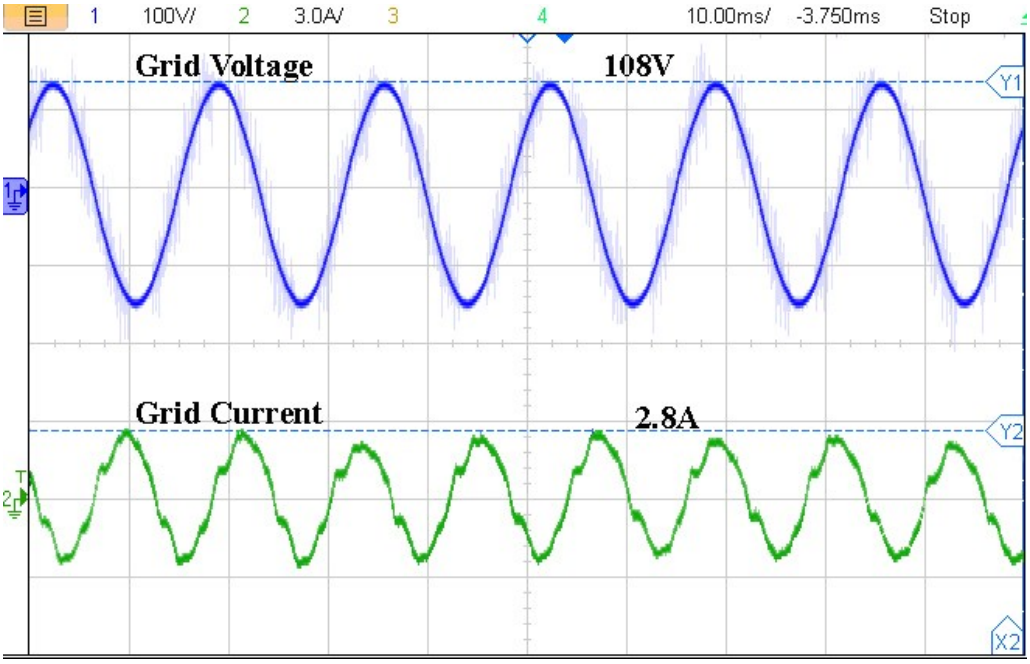

Figure 42: Grid voltage and current at PCC

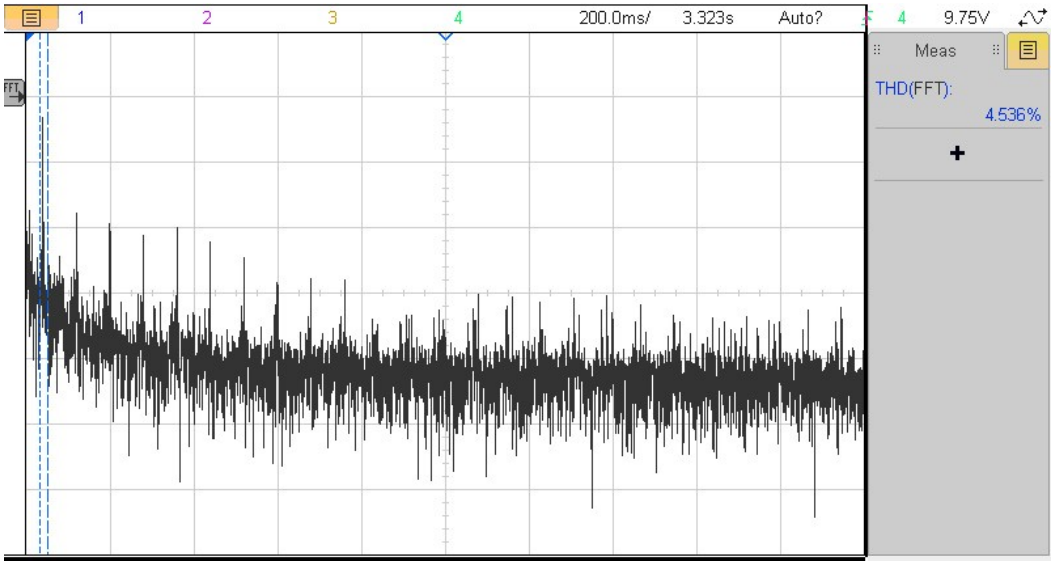

Figure 43: FFT analysis of grid current

4.4.4 Grid Behavior

Figure 42 presents the grid voltage and current waveforms for Scenario 1, Figure 43 provides the Fast Fourier Transform (FFT) analysis of the grid current, showing a THD of 4.5%. The average experimental efficiency of the system is measured at 93.75%, with an input power of 200W delivering an output of 187.5W. These results demonstrate the effectiveness of the proposed charging system in maintaining stable performance under varying load conditions.

4.5 Summary

The simulation and experimental results validate the feasibility of the proposed reconfigurable multiport EV FCS. The system demonstrated dynamic reconfiguration capabilities, enabling efficient charging of heavy, medium, and light EVs without the need for additional DC-DC converters.

The simulation results of 1 MVA EV FCS model confirmed stable operation under varying load conditions. The CHB controller maintained balanced output voltages at 1200 V per submodule, even during dynamic changes at t=1 s, t=2 s, and t=3 s. Voltage and current profiles of each EV battery validated system adaptability to EV demand changes. The charging ports provided by the proposed system are 200V(125A) for light EVs and 400V(250A) for medium EVs while reconfiguring the system for 800V(375A) ports for heavy EVs ensuring the dynamic performance of the proposed reconfiguration algorithm. Grid voltage and current at PCC remained stable, with THD kept below 5%, meeting IEEE 519-2022 standards.

The experimental results of the prototype demonstrated regulated voltage outputs and balancing performance at the outputs of three sub-modules of CHB converter. In Scenario 1, three light EVs were charged at 1.25 A per port, with each port maintaining 50 V and delivering 187.5 VA total power. In Scenario 2, a heavy EV charged at 2.5 A (100 V by series connecting port 1 and 2), while a light EV charged at 1.25 A (50 V at port 3). Total power delivery was 312.5 VA, with a voltage ripple of 8.2%. The balancing controller maintained stable 50 V outputs per submodule under varied loads. The overall system achieved an efficiency of 93.75%. The THD was observed to be below 5%.

Overall, the simulation and experimental results validate that the proposed system reliably manages dynamic power demands, maintains voltage stability, and ensures compliance with industry standards, proving its adaptability and robustness for fast-charging applications.

Chapter 5 Conclusions and Future Work

This thesis presents a groundbreaking approach to EV FCS through a reconfigurable multiport architecture that harnesses the capabilities of advanced SST technology. The primary innovation lies in providing multiple independent DC ports, overcoming the limitations of traditional shared DC bus architectures. An innovative reconfiguration strategy is introduced, utilizing a minimal number of switches to dynamically reconfigure ports, thereby enhancing operational resilience and ensuring robust performance under diverse load conditions.

A significant advancement of this research is the integration of a dynamic reconfiguration algorithm, enabling flexible port configurations to meet the varying charging needs of heavy, medium, and light EVs. This algorithm ensures optimal power delivery by dynamically adjusting voltage and current levels, promoting efficient resource utilization. The architecture also eliminates the need for additional DC-DC converters, as the DAB converter inherently supports independent DC buses with a wide range of charging currents. Thus, the proposed system significantly enhances the reliability, scalability, and cost-effectiveness of SST-based EV FCS within MV distribution grids.

Further, the validation of the proposed system was carried out through extensive simulation and experimental results. Simulations confirm the system's ability to maintain stable operation under dynamic load variations, with the CHB balancing controller consistently delivering output voltages of 1200 V per submodule. The system exhibited robust performance in EV charging operations, effectively managing the diverse power demands of heavy, medium, and light electric vehicles. Additionally, the results demonstrate grid stability at the PCC, maintaining current THD below 5% in compliance with IEEE 519-2022 standards. The experimental prototype further substantiates these findings, showcasing regulated voltage and current outputs for two distinct EV types. Synchronization across submodules verified the advanced control system's capability to balance voltages, even when power extraction varied in real-world scenarios. Notable achievements included peak power delivery of 312.5 VA, a voltage ripple of 8%, and an average efficiency of 93.75%. These results underscore the reliability, adaptability, and efficiency of the proposed system in both simulated and practical settings.

In conclusion, the proposed reconfigurable multiport EV FCS addresses critical challenges in EV charging infrastructure by offering a scalable, resilient, and cost-effective solution. Its dynamic reconfiguration capabilities, combined with independent DC buses and SST technology, ensure adaptability to diverse charging needs. The system's robust performance under dynamic conditions, and experimental validation underscore its readiness for real-world deployment. This work lays a solid foundation for future advancements in sustainable and efficient EV fast charging systems, aligning with the evolving demands of global EV adoption.

5.1 Thesis Contributions

This research makes several significant contributions to the development and validation of a reconfigurable, SST-based DC fast charging station for EVs.

A primary contribution of this work is the design and implementation of an SST-based DC charging station that utilizes independent DC buses. This architecture effectively addresses the challenges associated with conventional shared DC bus configurations, such as uneven power distribution, increased control complexity, and potential instability in multiport systems. By adopting independent DC buses, the proposed system enhances reliability, improves power flow management, and offers better isolation between charging ports, leading to more efficient and flexible operation.

The proposed system is presented as a general architecture that can be scaled up or down depending on power and voltage requirements. This scalability allows for seamless adaptation to different operational scenarios, ranging from small-scale charging facilities to high-power, utility-grade fast-charging stations. By ensuring modularity and flexibility, this research provides a foundation for future developments in EV charging infrastructure.

A major innovation introduced in this study is the development of a reconfigurable charging architecture, which significantly enhances the system’s adaptability. This architecture enables dynamic reallocation of power resources, allowing charging ports to be reassigned based on real-time demand. For instance, when a charging port is not being utilized by a light EV, it can be reconfigured to contribute partial power to a heavy EV.

This intelligent resource management optimizes power utilization, increases station efficiency, and enhances the overall flexibility of the charging infrastructure.

While independent DC bus-based topologies have been proposed in theoretical studies, no prior work has experimentally validated their feasibility. This research bridges that gap by implementing a scaled-down, single-phase experimental prototype to demonstrate the practicality of the independent DC bus approach. Through comprehensive testing, the study verifies the system's ability to efficiently charge multiple EVs while maintaining stable power distribution. The experimental results validate the effectiveness of the balancing and charging controllers, as well as the system's impact on grid stability in terms of voltage, current, and THD at the point of common coupling PCC.

The reconfigurable architecture proposed in this research maximizes resource utilization by ensuring that charging ports are not left idle when demand fluctuates. The ability to dynamically allocate power enhances the overall efficiency of the system, making it a cost-effective and practical solution for real-world applications. This contribution is particularly relevant for large-scale EV charging stations where efficient power management is critical to meeting the growing demand for fast and reliable charging services.

5.2 Future Work

Building on the foundations laid in this thesis, several avenues for future research and development can be explored to further enhance the proposed EV fast-charging system's performance as follows.

The experimental efficiency of the proposed system (93.75%) is observed to be comparable to traditional shared DC bus systems, with potential for improvement. The limited computational capabilities of the microcontroller restricted the switching frequency of the CHB converter, leading to higher-than-expected losses. Additionally, parasitic resistances and inductances within the experimental setup, coupled with poor thermal management, contributed to the reduced efficiency. Future efforts will focus on addressing these challenges by enhancing control hardware, optimizing the experimental setup to minimize

parasitic effects, and implementing improved thermal management solutions to achieve higher system efficiency.

Additionally, the experiment was conducted to verify that the proposed topology can deliver the required charging currents and voltages to the load after adjustments to the ports. However, due to time constraints, the real-time dynamic adjustment of the charging ports was not implemented experimentally. This aspect remains an open area for future research, where further work can focus on validating the real-time reconfiguration capabilities of the system under dynamic operating conditions.

Another suggestion for future work is to integrate the system with renewable energy sources such as solar PV and wind to enhance sustainability and reduce dependency on grid power. Advanced energy management strategies could be developed to dynamically allocate renewable energy to charging ports while maintaining voltage stability and synchronization across all modules.

Future research could also focus on refining grid interaction mechanisms to enable seamless bidirectional power flow for V2G, Grid-to-Vehicle (G2V), and Vehicle-to-Vehicle (V2V) operations. Advanced control strategies can be developed to optimize power factor correction, reduce peak load on the grid, and improve grid stability while leveraging EVs as distributed energy storage systems.

Additionally, the dynamic reconfiguration algorithm can be expanded to address increasingly complex charging scenarios, such as varying state-of-charge (SoC) requirements, including charging times and pricing. Advanced machine learning or AI-driven approaches could be employed to predict EV charging patterns, optimize resource allocation, and minimize energy wastage.

Moreover, ongoing advancements in SiC and GaN devices for SST applications can be leveraged to improve switching efficiency, thermal performance, and overall system compactness. These developments could allow for lighter, more efficient, and cost-effective SST designs, further optimizing the proposed architecture for commercial deployment.

By addressing these future research directions, the proposed system can evolve into a comprehensive, sustainable, and transformative solution for EV fast-charging infrastructure. This would not only meet the growing demands of the EV market but also align with global sustainability goals and the advancement of smart grid technologies.

References

[1] I. Energy Agency, "Global EV Outlook 2024 Moving towards increased affordability," 2024. [Online]. Available: www.iea.org

[2] S. S. G. Acharige, Md. E. Haque, M. T. Arif, N. Hosseinzadeh, K. N. Hasan, and A. M. T. Oo, "Review of Electric Vehicle Charging Technologies, Standards, Architectures, and Converter Configurations," *IEEE Access*, vol. 11, pp. 41218–41255, 2023.

[3] G. A. Abiassaf and A. A. Arkadan, "Impact of EV Charging, Charging Speed, and Strategy on the Distribution Grid: A Case Study," *IEEE Journal of Emerging and Selected Topics in Industrial Electronics*, vol. 5, no. 2, pp. 531–542, Apr. 2024.

[4] M. M. Mahfouz and M. R. Iravani, "Grid-Integration of Battery-Enabled DC Fast Charging Station for Electric Vehicles," *IEEE Transactions on Energy Conversion*, vol. 35, no. 1, pp. 375–385, Mar. 2020.

[5] V. T. Tran, Md. R. Islam, K. M. Muttaqi, and D. Sutanto, "An Efficient Energy Management Approach for a Solar-Powered EV Battery Charging Facility to Support Distribution Grids," *IEEE Trans Ind Appl*, vol. 55, no. 6, pp. 6517–6526, Nov. 2019.

[6] H. Arya and M. Das, "Fast Charging Station for Electric Vehicles Based on DC Microgrid," *IEEE Journal of Emerging and Selected Topics in Industrial Electronics*, vol. 4, no. 4, pp. 1204–1212, Oct. 2023.

[7] Y. Li, F. Qiu, Y. Chen, and Y. Hou, "Adaptive Distributionally Robust Planning for Renewable-Powered Fast Charging Stations Under Decision-Dependent EV Diffusion Uncertainty," *IEEE Trans Smart Grid*, vol. 15, no. 6, pp. 5853–5870, Nov. 2024.

[8] H. Cao, L. Du, F. Guo, Z. Ma, and Y. Zhao, "A Triple Active Bridge (TAB) Based Solid-State Transformer (SST) for DC Fast Charging Systems: Architecture and Control Strategy," in *2023 IEEE Energy Conversion Congress and Exposition (ECCE)*, IEEE, Oct. 2023, pp. 855–860.

[9] L. Tarisciotti, G. Buticchi, G. De Carne, J. Yang, C. Gu, and P. Wheeler, "Unified Cost Function Model Predictive Control for a three-stage Smart Transformer," in *2021 IEEE Energy Conversion Congress and Exposition (ECCE)*, IEEE, Oct. 2021, pp. 3468–3475.

[10] A. Ahmad, Z. Qin, T. Wijekoon, and P. Bauer, “An Overview on Medium Voltage Grid Integration of Ultra-Fast Charging Stations: Current Status and Future Trends,” *IEEE Open Journal of the Industrial Electronics Society*, vol. 3, pp. 420–447, 2022.

[11] E. J. Aladesanmi, R. Musumpuka, and D. G. Dorrell, “Multi-Port Power Electronic Transformer,” in *2021 IEEE Southern Power Electronics Conference (SPEC)*, IEEE, Dec. 2021, pp. 1–7.

[12] S. Jiang, C. Fan, N. Huang, Y. Zhu, and M. He, “A Fault Location Method for DC Lines Connected With DAB Terminal in Power Electronic Transformer,” *IEEE Transactions on Power Delivery*, vol. 34, no. 1, pp. 301–311, Feb. 2019.

[13] J. Zhang, Y. Zhang, J. Zhou, J. Wang, G. Shi, and X. Cai, “Control of a Hybrid Modular Solid-State Transformer for Uninterrupted Power Supply Under MVdc Short-Circuit Fault,” *IEEE Transactions on Industrial Electronics*, vol. 70, no. 1, pp. 76–87, Jan. 2023.

[14] A. Zabetian-Hosseini, G. Joos, and B. Boulet, “Distributed Control Design for V2G in DC Fast Charging Stations,” in *2021 IEEE Energy Conversion Congress and Exposition (ECCE)*, IEEE, Oct. 2021, pp. 655–661.

[15] Y. Jin, M. A. Acquah, M. Seo, and S. Han, “Optimal Siting and Sizing of EV Charging Station Using Stochastic Power Flow Analysis for Voltage Stability,” *IEEE Transactions on Transportation Electrification*, vol. 10, no. 1, pp. 777–794, Mar. 2024.

[16] R. De Seram, A. Golder, and S. S. Williamson, “Recent Advancements in Solid State Transformer-based EV Fast Charging Stations,” in *2023 IEEE 14th International Conference on Power Electronics and Drive Systems (PEDS)*, IEEE, Aug. 2023, pp. 1–6.

[17] G. Arena, A. Chub, M. Lukianov, R. Strzelecki, D. Vinnikov, and G. De Carne, “A Comprehensive Review on DC Fast Charging Stations for Electric Vehicles: Standards, Power Conversion Technologies, Architectures, Energy Management, and Cybersecurity,” *IEEE Open Journal of Power Electronics*, vol. 5, pp. 1573–1611, 2024.

[18] M. R. Khalid, I. A. Khan, S. Hameed, M. S. J. Asghar, and J. Ro, “A Comprehensive Review on Structural Topologies, Power Levels, Energy Storage Systems, and Standards for Electric Vehicle Charging Stations and Their Impacts on Grid,” *IEEE Access*, vol. 9, pp. 128069–128094, 2021.

[19] M. Z. Farooqi, B. Singh, and B. K. Panigrahi, “Integrated Electronic Capacitors-Based Split BES-Assisted Modular Multiport Power Electronic Transformer for Fast EV Charging Station,” *IEEE Transactions on Industrial Electronics*, vol. 71, no. 11, pp. 13578–13589, Nov. 2024.

[20] A. Ahmad, Z. Qin, T. Wijekoon, and P. Bauer, “An Overview on Medium Voltage Grid Integration of Ultra-Fast Charging Stations: Current Status and Future Trends,” *IEEE Open Journal of the Industrial Electronics Society*, vol. 3, pp. 420–447, 2022.

[21] A. Milczarek and M. Malinowski, “Comparison of Classical and Smart Transformers Impact on MV Distribution Grid,” *IEEE Transactions on Power Delivery*, vol. 35, no. 3, pp. 1339–1347, Jun. 2020.

[22] W. ur Rehman, J. W. Kimball, and R. Bo, “Multilayered Energy Management Framework for Extreme Fast Charging Stations Considering Demand Charges, Battery Degradation, and Forecast Uncertainties,” *IEEE Transactions on Transportation Electrification*, vol. 10, no. 1, pp. 760–776, Mar. 2024.

[23] M. Senol *et al.*, “Harmonics Measurement, Analysis, and Impact Assessment of Electric Vehicle Smart Charging,” *IEEE Open Journal of Vehicular Technology*, vol. 6, pp. 109–127, 2025.

[24] J.-M. Clairand, J. Rodruez-Garc, and C. Varez-Bel, “Assessment of Technical and Economic Impacts of EV User Behavior on EV Aggregator Smart Charging,” *Journal of Modern Power Systems and Clean Energy*, vol. 8, no. 2, pp. 356–366, 2020.

[25] R. P. Upputuri and B. Subudhi, “A Comprehensive Review and Performance Evaluation of Bidirectional Charger Topologies for V2G/G2V Operations in EV Applications,” *IEEE Transactions on Transportation Electrification*, vol. 10, no. 1, pp. 583–595, Mar. 2024.

[26] L. Wang, Z. Qin, T. Slangen, P. Bauer, and T. van Wijk, “Grid Impact of Electric Vehicle Fast Charging Stations: Trends, Standards, Issues and Mitigation Measures - An Overview,” *IEEE Open Journal of Power Electronics*, vol. 2, pp. 56–74, 2021.

[27] M. Mazumder and S. Debbarma, “EV Charging Stations With a Provision of V2G and Voltage Support in a Distribution Network,” *IEEE Syst J*, vol. 15, no. 1, pp. 662–671, Mar. 2021.

[28] L. Zheng *et al.*, “Solid-State Transformer and Hybrid Transformer with Integrated Energy Storage in Active Distribution Grids: Technical and Economic Comparison, Dispatch, and Control,” *IEEE J Emerg Sel Top Power Electron*, vol. 10, no. 4, pp. 3771–3787, Aug. 2022.

[29] P. Bravo, J. Pereda, M. M. C. Merlin, S. Neira, T. C. Green, and F. Rojas, “Modular Multilevel Matrix Converter as Solid-State Transformer for Medium and High Voltage AC Substations,” *IEEE Transactions on Power Delivery*, vol. 37, no. 6, pp. 5033–5043, Dec. 2022.

[30] M. A. Hannan *et al.*, “State of the Art of Solid-State Transformers: Advanced Topologies, Implementation Issues, Recent Progress and Improvements,” *IEEE Access*, vol. 8, pp. 19113–19132, 2020.

[31] D. Ronanki and S. S. Williamson, “Evolution of Power Converter Topologies and Technical Considerations of Power Electronic Transformer-Based Rolling Stock Architectures,” *IEEE Transactions on Transportation Electrification*, vol. 4, no. 1, pp. 211–219, Mar. 2018.

[32] R. De Seram, K. T. Lulbadda, T. Sidhu, and S. S. Williamson, “A Solid State Transformer-based Charging Station for Catering Heavy/Medium and Light Electric Vehicles,” in *2024 4th International Conference on Smart Grid and Renewable Energy (SGRE)*, IEEE, Jan. 2024, pp. 1–6.

[33] J. D. O. Pacheco, D. D. A. Honorio, and D. D. S. Oliveira, “An AC–DC Isolated MMC-Based Structure Suitable for MV SST Traction Applications,” *IEEE Access*, vol. 7, pp. 106395–106406, 2019.

[34] A. D. Bonde, P. Chaturvedi, V. B. Borghate, and C.-J. Chen, “Circulating Current Control (CCC) of Grid-Connected Hybrid Modular Multilevel Converter (MMC) for Solid State Transformer (SST) Application,” in *IECON 2023- 49th Annual Conference of the IEEE Industrial Electronics Society*, IEEE, Oct. 2023, pp. 1–6.

[35] Z. Jianqiao, Z. Jianwen, C. Xu, W. Jiacheng, and Z. Jiajie, “Family of Modular Multilevel Converter (MMC) Based Solid State Transformer (SST) Topologies for Hybrid AC/DC Distribution Grid Applications,” in *2018 IEEE International Power Electronics and Application Conference and Exposition (PEAC)*, IEEE, Nov. 2018, pp. 1–5.

[36] N. Kolli, S. Parashar, R. Kumar Kokkonda, S. Bhattacharya, and V. Veliadis, “Switching Loss Analysis of Three-Phase Three- Level Neutral Point Clamped Converter Pole Enabled by Series-Connected 10 kV SiC MOSFETs,” in *2023 IEEE Applied Power Electronics Conference and Exposition (APEC)*, IEEE, Mar. 2023, pp. 2353–2360.

[37] V. M. Iyer, S. Sharma, and S. Bhattacharya, “A Methodology to Select the Number of Cascaded Cells for a Medium Voltage Multilevel AC-DC Solid State Transformer,” in *2020 IEEE Transportation Electrification Conference & Expo (ITEC)*, IEEE, Jun. 2020, pp. 55–61.

[38] G. Jean-Pierre, A. K. Tripathi, V. Burugula, and V. Bhavaraju, “An Optimized Start-up Scheme for Isolated Cascaded AC/DC Power Converters,” in *2022 IEEE Energy Conversion Congress and Exposition (ECCE)*, IEEE, Oct. 2022, pp. 1–6.

[39] E. S. Lee, J. H. Park, M. Y. Kim, and J. S. Lee, “High-Efficiency Module Design of Solid-State Transformers for Railway Vehicles,” *IEEE Transactions on Transportation Electrification*, vol. 8, no. 1, pp. 98–120, Mar. 2022.

[40] A. Anurag, S. Acharya, S. Bhattacharya, T. R. Weatherford, and A. A. Parker, “A Gen-3 10-kV SiC MOSFET-Based Medium-Voltage Three-Phase Dual Active Bridge Converter Enabling a Mobile Utility Support Equipment Solid State

Transformer," *IEEE J Emerg Sel Top Power Electron*, vol. 10, no. 2, pp. 1519–1536, Apr. 2022.

[41] P. Apte, S. Lin, L. Frager, and J. Friebe, "Design Considerations for a 50 kW Dual Bridge Series Resonant DC/DC Converter with Wide-Input Voltage Range for Solid-State Transformers," in *2021 IEEE Energy Conversion Congress and Exposition (ECCE)*, IEEE, Oct. 2021, pp. 1164–1170.

[42] M. Hatatah and B. M. Grainger, "Power and Voltage regulation of a Solid-State Transformer based Quad-Active Bridge DC–DC Converter using Adaptive Linear Quadratic Regulator and Nonlinear Model Predictive Control," in *2020 IEEE Energy Conversion Congress and Exposition (ECCE)*, IEEE, Oct. 2020, pp. 1623–1629.

[43] R. De Seram, K. T. Lulbadda, T. Sidhu, and S. S. Williamson, "A Quad-Active Bridge (QAB)-Based Solid-State Transformer for Fast Charging of Light/Medium and Heavy Electric Vehicles," in *2024 IEEE International Conference on Industrial Technology (ICIT)*, IEEE, Mar. 2024, pp. 1–6.

[44] A. Nigam and D.-C. Lee, "Replacement of Arm Inductors by Leakage Inductance of Input Transformers in QAB-CLLC-Based MMC," in *2023 11th International Conference on Power Electronics and ECCE Asia (ICPE 2023 - ECCE Asia)*, IEEE, May 2023, pp. 2253–2258.

[45] J. Saha, G. N. Brahmendra Yadav, and S. Kumar Panda, "A Bidirectional Matrix-Based AC-DC Dual-Active Bridge for Modular Solid-State-Transformers," in *IECON 2020 The 46th Annual Conference of the IEEE Industrial Electronics Society*, IEEE, Oct. 2020, pp. 1136–1141.

[46] J. Saha, N. Kumar, and S. K. Panda, "A Futuristic Silicon-Carbide (SiC)-Based Electric-Vehicle Fast Charging/Discharging (FC/dC) Station," *IEEE J Emerg Sel Top Power Electron*, vol. 11, no. 3, pp. 2904–2917, Jun. 2023.

[47] V. M. Iyer, S. Gulur, G. Gohil, and S. Bhattacharya, "An Approach Towards Extreme Fast Charging Station Power Delivery for Electric Vehicles with Partial Power Processing," *IEEE Transactions on Industrial Electronics*, vol. 67, no. 10, pp. 8076–8087, Oct. 2020.

[48] A. C. Nair and B. G. Fernandes, "Solid-State Transformer Based Fast Charging Station for Various Categories of Electric Vehicles With Batteries of Vastly Different Ratings," *IEEE Transactions on Industrial Electronics*, vol. 68, no. 11, pp. 10400–10411, Nov. 2021.

[49] N. D. Dao, H. V. Nguyen, and D.-C. Lee, "Semi-Modular Solid-State Transformers With Reduced Count of Components Based on Single-Stage AC/DC Converters," *IEEE Trans Power Electron*, vol. 37, no. 7, pp. 8177–8189, Jul. 2022.

[50] L. Zheng, R. P. Kandula, and D. Divan, “Multiport Control With Partial Power Processing in Solid-State Transformer for PV, Storage, and Fast-Charging Electric Vehicle Integration,” *IEEE Trans Power Electron*, vol. 38, no. 2, pp. 2606–2616, Feb. 2023.

[51] D. Choi, J.-H. Park, and J.-S. Lee, “Individual Module Power Transmission Control for Extreme Fast Charging Stations Configured With Solid-state Transformer,” in *2023 IEEE Applied Power Electronics Conference and Exposition (APEC)*, IEEE, Mar. 2023, pp. 1723–1728.

[52] Z. Ni *et al.*, “A New Approach to Input Filter Design for Regenerative Cascaded H-Bridge Drives,” *IEEE Transactions on Industrial Electronics*, vol. 69, no. 4, pp. 3266–3277, Apr. 2022.

[53] S. Nayak and A. Das, “A DAB based Folder-Unfolder circuit in Cascaded H-Bridge Converter for MV Grid Application,” in *2022 IEEE International Conference on Power Electronics, Drives and Energy Systems (PEDES)*, IEEE, Dec. 2022, pp. 1–6.

[54] S. Zengin and M. Boztepe, “A Novel Current Modulation Method to Eliminate Low-Frequency Harmonics in Single-Stage Dual Active Bridge AC–DC Converter,” *IEEE Transactions on Industrial Electronics*, vol. 67, no. 2, pp. 1048–1058, Feb. 2020.

[55] J. Yin, J. Lu, Y. Liu, J. Peng, and H. Jiang, “Novel Phase-Shift Method for Fast Power Reversal With Transient Zero Voltage Switching in a Bidirectional Dual Active Bridge DC–DC Converter,” *IEEE Transactions on Industrial Electronics*, vol. 68, no. 9, pp. 8028–8038, Sep. 2021.

[56] R. De Seram, K. T. Lulbadda, T. Sidhu, and S. S. Williamson, “An In-depth Comparative Analysis and Efficiency Evaluation of Dual- and Quad-active Bridge for Solid State Transformer Applications,” in *2024 IEEE Transportation Electrification Conference and Expo (ITEC)*, IEEE, Jun. 2024, pp. 1–6.

[57] A. Anurag, S. Acharya, S. Bhattacharya, T. R. Weatherford, and A. A. Parker, “A Gen-3 10-kV SiC MOSFET-Based Medium-Voltage Three-Phase Dual Active Bridge Converter Enabling a Mobile Utility Support Equipment Solid State Transformer,” *IEEE J Emerg Sel Top Power Electron*, vol. 10, no. 2, pp. 1519–1536, Apr. 2022.

[58] O. Cipriano da Silva, F. L. Tofoli, D. Honorio, L. H. Barreto, and D. de S. Oliveira, “Single-Phase Isolated AC-AC Converters Based on the Dual Active Bridge Converter,” *IEEE Transactions on Industrial Electronics*, vol. 69, no. 6, pp. 5680–5689, Jun. 2022.

[59] Y. Zhou and B. Luo, “Optimal design of 6kw high frequency transformer using AP method,” in *2023 IEEE 4th China International Youth Conference On Electrical Engineering (CIYCEE)*, IEEE, Dec. 2023, pp. 1–5.

[60] S. Joseph, A. K. Abraham, P. Harikrishna Raj, J. Joseph, and K. R. M. Nair, “An Iterative Algorithm for Optimum Design of High Frequency Transformer in SST Application,” in *IECON 2020 The 46th Annual Conference of the IEEE Industrial Electronics Society*, IEEE, Oct. 2020, pp. 1538–1543.

[61] F. Wu, T. Guo, Y. Ai, S. Chen, J. Liu, and Y. An, “Research on the Design Method of Nanocrystalline High-Frequency Transformer,” in *2024 International Conference on HVDC (HVDC)*, IEEE, Aug. 2024, pp. 670–675.

[62] R. A. G. Jimenez, G. G. Oggier, R. A. Fantino, J. C. Balda, and Y. Zhao, “Design of Nanocrystalline Medium-Voltage Medium-Frequency Three-Phase Transformers for Grid-Connected Applications,” in *2021 IEEE Energy Conversion Congress and Exposition (ECCE)*, IEEE, Oct. 2021, pp. 1142–1148.

[63] H. Wen, Y. Liu, D. Jiao, C.-S. Yeh, and J.-S. Lai, “Design Principles and Optimization Considerations of a High Frequency Transformer in GaN Based 1 MHz 2.8 kW LLC Resonant Converter with over 99% Efficiency,” in *2021 IEEE Applied Power Electronics Conference and Exposition (APEC)*, IEEE, Jun. 2021, pp. 1939–1944.

[64] S. Shao *et al.*, “Modeling and Advanced Control of Dual-Active-Bridge DC–DC Converters: A Review,” *IEEE Trans Power Electron*, vol. 37, no. 2, pp. 1524–1547, Feb. 2022.

[65] Q. Bu, H. Wen, H. Shi, and Y. Zhu, “A Comparative Review of High-Frequency Transient DC Bias Current Mitigation Strategies in Dual-Active-Bridge DC–DC Converters Under Phase-Shift Modulations,” *IEEE Trans Ind Appl*, vol. 58, no. 2, pp. 2166–2182, Mar. 2022.

Appendices

Appendix A.

Publications

Journal Papers

1. **R. De Seram**, K. T. Lulbadda, Oruganti V.S.R.Varaprasad and S. S. Williamson. “Reconfigurable Multiport Solid-State Transformer for DC Fast Charging Stations”, *IEEE Journal of Emerging and Selected Topics in Power Electronics (JESTPE)*, December 2024. (Under Review)

2. A. Golder, K. Lulbadda, **R. De Seram**, T. Sidhu; S. Williamson, “Rule-Based Energy Management System for Vehicle-to-Vehicle Power Sharing”, *IEEE Transactions on Industry Application (IAS)*, August 2024. (Under Review)

Prints

1. K.T. Lulbadda, A. Golder and **R. De Seram,** “Chapter 5: Electric Vehicle as Decentralized Energy Storage System,” in *Technologies and Applications of Batteries, Smart Charging, and Advanced Battery Management Systems for E-mobility*, A. Samanta and S. Williamson, River Publishers, 2024. (Under Review)
2. K.T. Lulbadda, A. Golder and **R. De Seram,** “Smart Grid Communication and Protocols and Smart Integration of EVs,” *in Electric Vehicle and Distributed Generation - Microgrid*, A. Samanta and S. Williamson, River Publishers, 2024. (Under Review)

Conference Proceedings

1. K. T. Lulbadda, **R. D. Seram**, O. V. S. R. Varaprasad, T. Sidhu, and S. S. Williamson, "Design and Analysis of a Bi-directional Solid-State Battery Protection System for Solid-State Transformer Based Grid Supporting EV Charging Systems", IEEE Transportation Electrification Conference & Expo+ Electric Aircraft Technologies Symposium (ITEC+), Anaheim, CA, USA, 2025. (Accepted)
2. **R. De Seram**, K. T. Lulbadda, O. V. S. R. Varaprasad, and S. S. Williamson, “An Analysis of Single- and Dual-Phase Shift Modulation Techniques for Closed-loop Control of Dual-Active Bridge”, *Annual Conference of the IEEE Industrial Electronics Society (IECON)*, Chicago, Illinois, USA, 2024.
3. K. T. Lulbadda, **R. D. Seram**, T. Sidhu, and S. S. Williamson, "Analysing the Behavior of Solid State Protection System for Dual Active Bridge in Solid State Transformers Under Short Circuit Faults", IEEE Energy Conversion Congress & Expo (ECCE), Phoenix, Arizona, USA, 2024.
4. **R. De Seram**, K. T. Lulbadda, T. Sidhu and S. S. Williamson, "An In-depth Comparative Analysis and Efficiency Evaluation of Dual- and Quad-active Bridge for Solid State Transformer Applications," *2024 IEEE Transportation Electrification Conference and Expo (ITEC)*, Chicago, IL, USA, 2024, pp. 1-6.
5. **R. De Seram**, K. T. Lulbadda, T. Sidhu and S. S. Williamson, "A Quad-Active Bridge (QAB)-Based Solid-State Transformer for Fast Charging of Light/Medium and Heavy Electric Vehicles," *2024 IEEE International Conference on Industrial Technology (ICIT)*, Bristol, United Kingdom, 2024, pp. 1-6.

6. K. T. Lulbadda, **R. De Seram**, T. Sidhu and S. S. Williamson, "The Behavior of DC Microgrid Connected Solid State Transformer During Internal Short Circuits," *2024 IEEE International Conference on Industrial Technology (ICIT)*, Bristol, United Kingdom, 2024, pp. 1-6
7. **R. De Seram**, K. T. Lulbadda, T. Sidhu and S. S. Williamson, "A Solid-State Transformer-based Charging Station for Catering Heavy/Medium and Light Electric Vehicles," 2024 4th International Conference on Smart Grid and Renewable Energy (SGRE), Doha, Qatar, 2024, pp. 1-6.
8. K. T. Lulbadda, **R. D. Seram**, T. Sidhu and S. S. Williamson, "Protection Schemes of Solid State Transformers for Different Fault Conditions," *2024 4th International Conference on Smart Grid and Renewable Energy (SGRE)*, Doha, Qatar, 2024, pp. 1-6.
9. **R. De Seram**, A. Golder, and S. S. Williamson, "Recent Advancements in Solid State Transformer-based EV Fast Charging Stations," 2023 IEEE 14th International Conference on Power Electronics and Drive Systems (PEDS), Montreal, QC, Canada, 2023, pp. 1-6.
10. K. T. Lulbadda, **R. De Seram**, N. Shrestha, T. Sidhu and S. S. Williamson, "An Analysis of Advanced Soft-Switching Techniques for DC–AC Power Converters Based on Auxiliary Circuits," *2023 IEEE International Conference on Industrial Technology (ICIT)*, Orlando, FL, USA, 2023, pp. 1-6.